Aeolian Research 57 (2022) 100812

Contents lists available at ScienceDirect

Aeolian Research

journal homepage: www.elsevier.com/locate/aeolia

Surface-area development of foredune trough blowouts and associated parabolic dunes quantified from time series of satellite imagery

Niels van Kuik [a,b], Job de Vries [a], Christian Schwarz [a,c], Gerben Ruessink [a,*]

[a] Department of Physical Geography, Faculty of Geosciences, Utrecht University, P.O. Box 80.115, 3508 TC Utrecht, The Netherlands
[b] Now at Rijkswaterstaat, Water Verkeer en Leefomgeving, Utrecht, The Netherlands
[c] Department of Civil Engineering, KU Leuven, Belgium

ARTICLE INFO

Keywords:
Blowouts
Beach-dune interaction
Bio-geomorphology
Google Earth Engine
Linear spectral unmixing

ABSTRACT

Foredune trough blowouts are elongated wind-eroded depressions in the most seaward dune and their adjoining depositional lobes. Despite their importance to the sand budget and floral diversity of coastal dunes, the spatiotemporal evolution of trough blowouts is not well understood. We designed an automated workflow in the Google Earth Engine platform to produce time series of blowout surface area from medium-resolution satellite imagery available since the mid-1980s and applied it to a blowout system in the Netherlands, Denmark and the USA. Blowout surface areas were found to vary on multi-annual, seasonal and episodic time scales. Multi-annual change reflects successive development through stages of growth, stabilization and decay. The transition from growth to stabilization appears to be related to a change in blowout shape (width-to-length ratio). The decay phase starts with vegetation obstructing the blowout connection to the beach; the lobe can still migrate inland and develop into a parabolic dune before also becoming fully vegetated. The seasonal variations in blowout area increase with latitude; the observed larger areas in winter at the Dutch and Danish site presumably reflect seasonal plant development and the effect of stronger winds in winter. Episodic increases in blowout area, observed during winter at the Danish site only, are associated with pronounced foredune erosion. None of the episodic events changed blowouts into a different stage or persistently affected seasonal dynamics. Future work should focus on the combined analysis of changes in blowout area and sand volume to improve our understanding of sand-vegetation interactions driving blowout dynamics.

1. Introduction

Foredune blowouts are localized wind-eroded depressions in the most seaward coastal dune together with their adjoining depositional lobes (Carter et al., 1990; Hesp, 2002). They have been documented at numerous dune coasts worldwide (e.g, Hesp and Walker, 2013; Schwarz et al., 2019), mostly in a saucer-, bowl- or trough-shaped morphological configuration (e.g., Ritchie, 1972; Carter et al., 1990; Hesp, 2002; Mir-Gual et al., 2013; Abhar et al., 2015). Saucer blowouts have a shallow semi-circular dish-shaped deflation basin and sometimes evolve in the deeper bowl blowouts. Trough blowouts are generally characterized by an elongated trough with often steep lateral sidewalls and a deep well-developed deflation basin with an opening at the beach side and a depositional lobe at its landward side. Especially trough blowouts play an essential role in the sand budget of many coastal dune systems. They can act as effective conduits for aeolian transport (Carter et al., 1990; Byrne, 1997; Davidson-Arnott, 2005; Anderson and Walker, 2006; Nordstrom et al., 2007; Ruessink et al., 2018) between the beach and the backdune and facilitate washovers at low foredune systems (Jewell et al., 2017). In addition, blowouts affect dune vegetation (e.g., Hesp, 1991; Maun, 1998). While excessive bed level change will increase plant mortality, moderate sand accumulation may instead lead to local vegetation rejuvenation (e.g., Arens et al., 2013; Kuipers, 2014; Schwarz et al., 2019) and hence an overall larger floristic diversity than in dunes without blowouts (Nordstrom et al., 2007; Laporte-Fauret et al., 2021). In Northwestern Europe and New Zealand, nature and coastal managers are experimenting with excavating trough blowout-like gaps through densely vegetated foredune systems (Riksen et al., 2016; Pye and Blott, 2017; Ruessink et al., 2018; Castelle et al., 2019; Nguyen et al., 2022) in the hope that a positive sand budget beyond the foredune in concert with enlarged biodiversity improves coastal resilience in times of human-induced global change (e.g., Kuipers, 2014; Arens et al., 2020;

* Corresponding author.
E-mail address: b.g.ruessink@uu.nl (G. Ruessink).

https://doi.org/10.1016/j.aeolia.2022.100812
Received 4 November 2021; Received in revised form 18 May 2022; Accepted 10 June 2022
Available online 22 June 2022

Pye et al., 2020; Laporte-Fauret et al., 2021). Despite the common occurrence of trough blowouts in natural foredunes and their excavation as part of nature-based management schemes, the evolution of trough blowouts and the associated spatiotemporal scales are not well understood.

Trough blowouts evolve due to the feedback between abiotic (physical) and biotic (biological) processes on time scales ranging from strong wind event, seasons, to multiple decades. Building on earlier work (Carter et al., 1990; Gares, 1992; Gares and Nordstrom, 1995; Hesp, 2002; Corenblit et al., 2015), Schwarz et al. (2019) linked trough blowout initiation, development and closure in a conceptual manner to spatial and temporal variability in the dominance of abiotic and biotic processes and the strength of their interaction (Fig. 1). Starting with a small vegetation-free depression in the foredune, which may result from foredune scarping during a storm surge (Hesp, 2002; Castelle et al., 2017), blowout initiation is driven by airflow-accelerated erosional sand transport processes (Hesp and Hyde, 1996; Pease and Gares, 2013; Smyth et al., 2013) that increase blowout depth and width. Schwarz et al. (2019) called this stage of blowout evolution, which is dominated by physical processes, the geomorphological stage (Fig. 1). As the blowout develops further, airflow is accelerated less and consequently, there are fewer physical disturbances. This will allow early successional species to colonize the blowout and lobe edges (e.g., Laporte-Fauret et al., 2021). The species will engineer their environment. In this stage, abiotic and biotic processes thus strongly interact in shaping the blowout; hence, this stage was called the bio-geomorphological stage (Fig. 1). In the final, ecological stage (Fig. 1), the vegetation spreads further over the deflation basin, eventually leading to blowout closure and infilling as well as vegetation succession (Gares and Nordstrom, 1995; Hesp, 2002; Battiau-Queney, 2014). The blowout lobe may continue to migrate inland in the prevailing wind direction (Jewell et al., 2017) and evolve into a 'U' or 'V' shaped parabolic dune with its characteristic upwind pointing, marginal ridges stabilized by vegetation (Carter et al., 1990; Hesp, 2002; Hesp and Walker, 2013; Yan and Baas, 2015). Even though Schwarz et al. (2019)'s conceptual three-stage succession model still needs to be tested on real foredune trough-blowout systems, it seems unlikely that a trough blowout will progress in a simple linear manner through the three stages over time. The non-linear nature of bio-geomorphical feedbacks and the possibility of tipping points, together with time-varying meteorological forcing (e.g., rainfall, wind speed and direction), may result in highly complicated trajectories for blowout development which can last for decades (e.g., Gares and Nordstrom, 1995; Hesp, 2002; Dech et al., 2005; Jewell et al., 2017). This long time scale also has implications for the dune management strategy that involves blowout excavation.

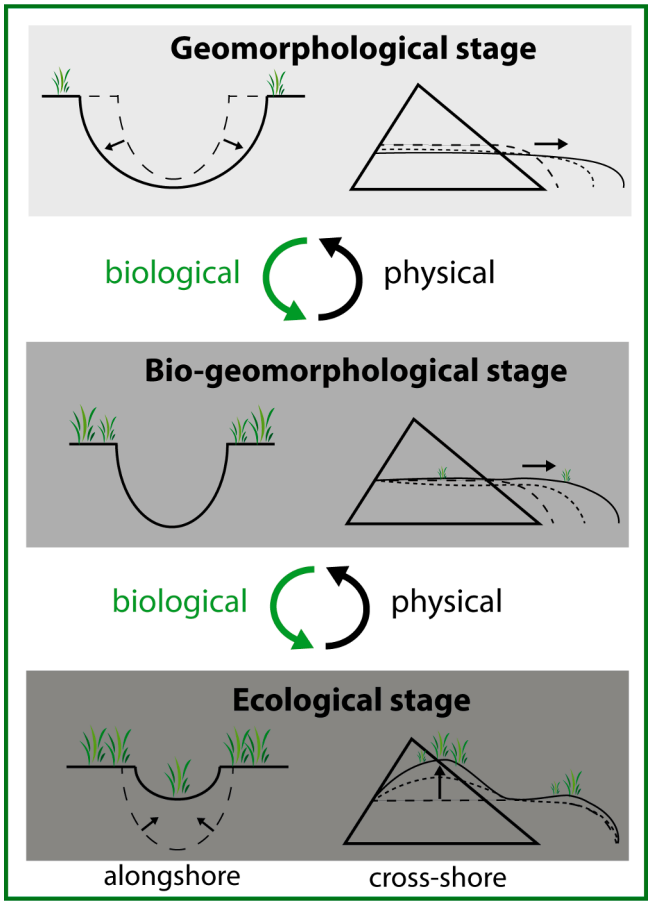

Fig. 1. Schematic diagram of the three-stage blowout-evolution model proposed by Schwarz et al. (2019). The three panels illustrate the morphological evolution during the geomorphological, bio-geomorphological and ecological stage viewed in the onshore (deflation basin; left column) and alongshore (depositional lobe; right column). Line signatures and small arrows indicate development over time within a stage. The large arrows between the panels indicate stage transitions because of biological (biotic) and physical (abiotic) processes. See text for further explanation.

The exisiting scarce observational blowout research on time scales of multiple years or longer (e.g., Jungerius and Van der Meulen, 1989; Gares and Nordstrom, 1995; Dech et al., 2005; Abhar et al., 2015; Jewell et al., 2017; Ruessink et al., 2018; Smyth et al., 2020) has often been based on digital elevation models or aerial photographs at a single site with a coarse temporal resolution, that is, with a maximum of two or three observations per year, but more commonly with multiple years between observations. This precludes studying how blowouts respond to individual disturbances such as a major wind event or change in response to seasonality in wind forcing (e.g., Byrne, 1997) and plant phenology. Also, it remains unclear which processes drive long-term changes in blowout stage and whether stage transitions are abrupt or gradual. The public availability of medium-resolution (10–60 m) satellite imagery since 1984, accompanied with major developments in visualization and processing (e.g., Huntington et al., 2017) and cloud computation power such as Google Earth Engine (GEE; Gorelick et al. (2017)), has facilitated local to global, daily to decadal assessments of coastal change, with applications to sandy beaches (e.g., Luijendijk et al., 2018; Vos et al., 2019), coastal dunes (Jackson et al., 2019), tidal flats (Murray et al., 2019), subtidal mudbanks (De Vries et al., 2021) and mangroves (e.g., Yancho et al., 2020). We believe that the free availability of medium-resolution satellite imagery offers a new means of studying foredune blowout dynamics that overcomes many of the aforementioned limitations.

The aim of this study is to quantify the temporal evolution of the surface area of selected foredune trough blowouts and associated parabolic dunes worldwide from medium-resolution multi-spectral satellite imagery available in the GEE platform with a focus on gradual (multi-annual) and seasonal (intra-annual) change. We first created an algorithm inside GEE to produce time series of blowout surface area at a given site. Because the size of many sand and vegetation patches in blowout systems is below the sensor resolution, especially near the edges of the deflation basin and the depositional lobe, a linear spectral unmixing model (Keshava and Mustard, 2002; Ettrich et al., 2018) is the key element of the developed algorithm. We then applied the algorithm to foredune trough-blowout systems at Zuid-Kennemerland, the Netherlands; at Skodbjerge, Denmark; and at Padre Island, Texas, USA, where parabolic dunes also occur (McKenna, 2007). The sites were selected because they differ in the number, size, age and origin of the blowouts, foredune characteristics as well as climatic setting with associated differences in the mean and time-varying wind characteristics. Several high-resolution (1 m) orthomosaics previously acquired with an Unoccupied Aerial Vehicle at the Zuid-Kennemerland study site (Ruessink et al., 2018) were used to test the accuracy of the developed algorithm. In the Discussion section we put the obtained time series in

the context of the bio-geomorphological blowout model of Schwarz et al. (2019) and address some methodological issues of the designed algorithm.

2. Study sites

2.1. Zuid-Kennemerland, the Netherlands

In Zuid-Kennemerland (Fig. 2), five gaps were excavated in winter 2012–2013 through an approximately 900-m long section of the 20-m high, densely vegetated foredune as part of an EU-funded management strategy to stimulate aeolian dynamics in the coastal dunes (Kuipers, 2014). The anthropogenic gaps were initially 50–100 m wide and 100–200 m long (in the cross-shore), with an excavation depth of 9 to 12.5 m. Based on a series of digital elevation maps, Ruessink et al. (2018) illustrated how the gaps quickly evolved into naturally looking trough blowouts with well-developed deflation basins, steep and eroding lateral walls as well as depositional lobes, which locally became 8-m thick and grew inland by up to 50 m/year. The northern two blowouts are aligned with the dominant southwesterly wind direction (Fig. 3), while the southern three blowouts are oriented approximately shore-normally. The strongest winds (up to 25 m/s) are from the southwest or the northwest (Fig. 3), and are mostly limited to the winter months November to February. The northwesterly winds are often associated with substantial storm surges that can result in dune scarping (e.g., De Winter et al., 2015) but because of the wide low-sloping beach fronting the blowouts, dune erosion at the Zuid-Kennemerland coast is rare.

2.2. Skodbjerge, Denmark

The second European site is the blowout system just to the south of the vacation resort Haurvig, in the region Skodbjerge along the southern part of the narrow spit Holmsland Tange on the western coast of Denmark (Fig. 2). The coastline is almost north–south orientated (≈ 355°N). The foredunes are about 13 to 15 m high and intersected by several closely spaced blowouts, with depositional lobes extending to 500 m inland. Annual airborne Lidar surveys collected since 2005 show that the region is geomorphologically highly dynamic (Karlsson and Larsen, 2020). Aeolian erosion is mainly concentrated along the seaward foredune slope and in the deflation basin of the blowouts, with the eroded sand primarily deposited landward of the foredune crest and on the depositional lobes. Furthermore, over the years several individual blowouts and depositional lobes merged into a large (in the alongshore) blowout and an associated sand sheet (Karlsson and Larsen, 2020). The blowouts near Skodbjerge are oriented to the southeast, aligned with the dominant northwesterly winds (Fig. 3) but blowouts elsewhere along the Holmsland Tange spit (not included in the present study) have a more shore-normal orientation (Karlsson and Larsen, 2020). The strongest winds are from the west and northwest, and can exceed 30 m/s. The associated high storm surge levels and wave heights (up to 7.5 m) can cause scarping of the foredune along the Holmsland Tange spit (Earnshaw and Madsen, 2014; Karlsson and Larsen, 2020).

2.3. Padre Island, Texas, USA

Padre Island, Texas, is a barrier island along the western side of the

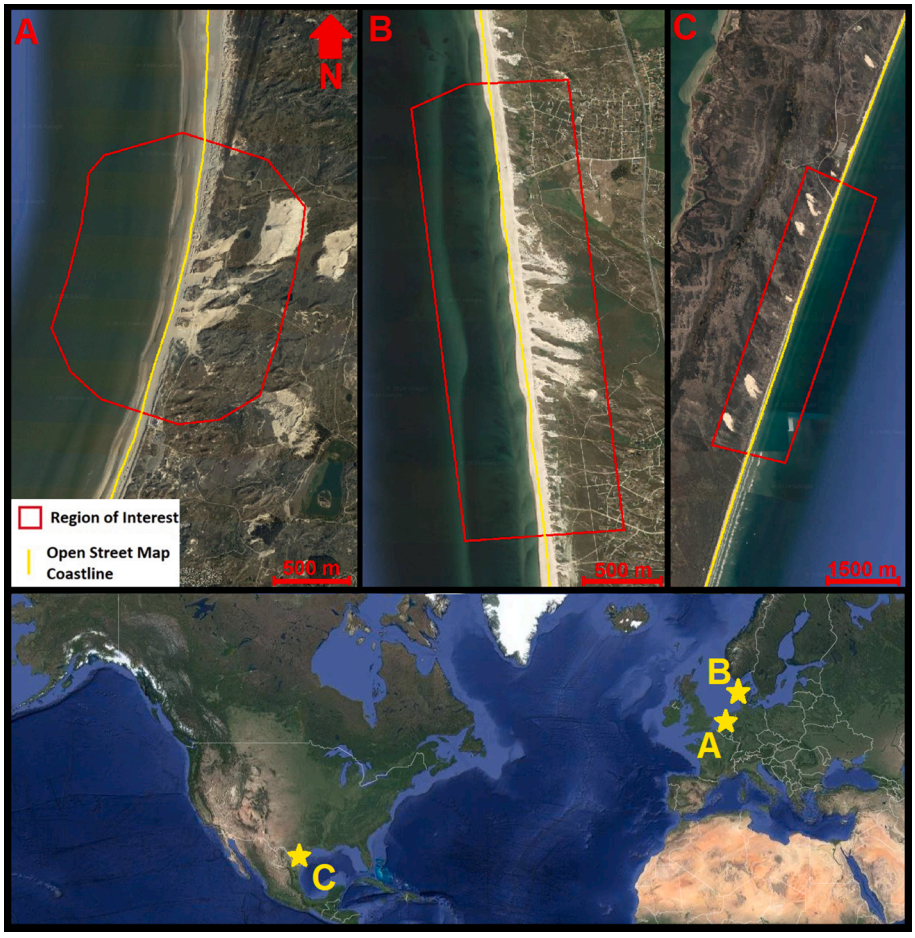

Fig. 2. Google Earth imagery of the study sites: A, Zuid-Kennemerland, the Netherlands (April 2019); B, Skodbjerge, Denmark (July 2018); C, Padre Island, USA (February 2020). The yellow line in panels A–C is the OpenStreetMap coastline. The red line outlines the region of interest, or ROI; see Section 3.2.

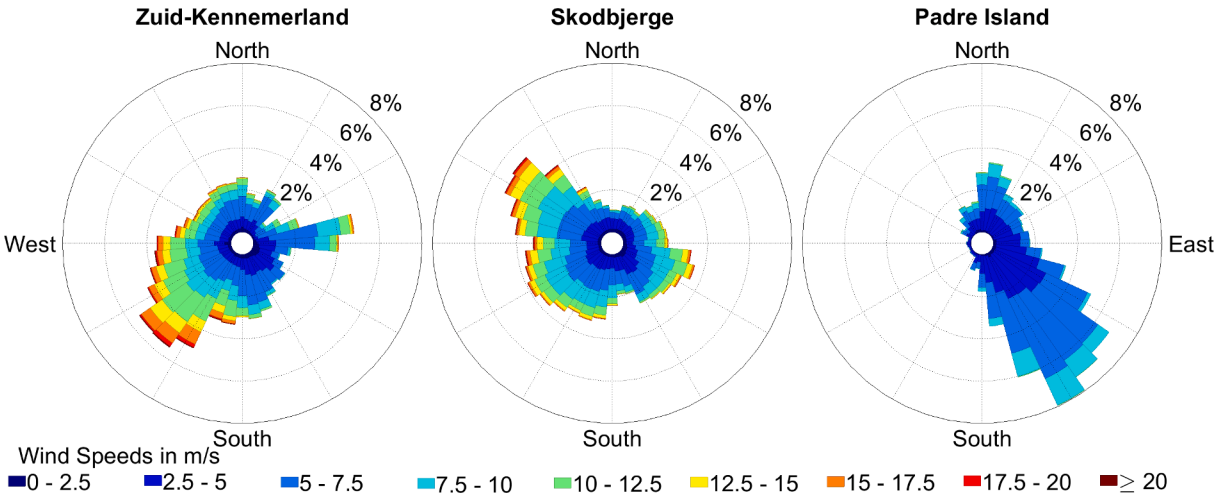

Fig. 3. Wind roses for (from left to right) Zuid-Kennemerland, Skodbjerge and Padre Island. The data shown for Zuid-Kennemerland were measured approximately 4-km to the north of the study site on the IJmuiden harbour mole, at 10-m height between January 2012 and May 2020. Data for Skodbjerge were collected some 13 km to the north in the harbour town of Hvide Sande, at a height of 25 m, between 1980 and 2020. Data for Padre Island were measured at the Corpus Cristi N.A.S. Airport weather station, at a height of 5.5 m, between 1980 and 2020 (data were missing for 1998–2000 and 2002–2006).

coast of the Gulf of Mexico (Fig. 2). The ≈ 3.5-m high foredune is intersected by several blowouts in a stretch of coast where beach driving is permitted. It has been argued (Houser et al., 2013; Jewell et al., 2017) that this driving alters beach and dune-toe characteristics in such a way that the foredune has become more susceptible to scarping and overwash during extreme storms (hurricanes), thereby initiating and reactivating blowouts. Blowout characteristics and behaviour at the site have been analysed previously by Jewell et al. (2015) and Jewell et al. (2017) for the period 1969 – 2010 based on limited (temporal resolution) aerial and satellite imagery supplemented with Lidar surveys and ground-penetrating radar data. Blowout widths at the beach were shown to range between 25 and 60 m, with the more inland parts being wider, up to 200 m. The cross-shore length of the blowouts varied between 140 and 430 m. Several blowouts lost their connection to the beach, with the lobes subsequently evolving into parabolic dunes (see Fig. 2C and McKenna (2007)) and migrating inland at an average speed of 150 m y^{-1} (Jewell et al., 2015). The climate along the Texas coast is characterized by hot (over 30 °C) summers and almost year-round arid conditions; only during fall (September and October), the rainfall on average exceeds 100 mm per month. The strongest winds tend to come from the south east to south (Fig. 3) and occur mainly during spring and summer. The hurricane season is from June till November.

3. Methodology

3.1. Initial considerations

In order to compute time series of blowout surface area at the three study sites we developed an algorithm that we applied in the cloud-computing environment of Google Earth Engine on the medium-resolution Landsat-4, -5, -7, -8 (30 m) and Sentinel-2 (10 m) top-of-atmosphere products. The increased revisit period from 16 days (Landsat 4–8; 1984–present) to 5 days (Sentinel-2; 2015–present) has resulted in a substantial increase in the number of available images with time, especially since 2017 with the launch of the second Sentinel-2 satellite. The number of images available in GEE for Skodbjerge, for example, varied between 10 and 20 per year for the period 1982–1998 (Landsat 4–5 only), and was near 190 in 2018 and 2019. Not all images are usable, however, because of the presence of clouds or cloud shadows, and these must be removed before further processing.

Cloudfree satellite images of coastal dune systems can generally be categorized in three main cover types: water (sea, dune slacks), vegetation and bare sand. Because of the medium spatial resolution of the images, most land pixels will often contain more than one cover type and their reflectance spectrum is thus a composite of the spectra of the separate cover types. Linear spectral unmixing (LSU) is a commonly applied technique to decompose the measured spectrum of a mixed pixel into the fractional abundances of each cover type (Keshava and Mustard, 2002); see Ettrich et al. (2018) for an LSU application to coastal dune systems. A critical step in performing LSU is to find the spectra of each cover type (or, endmember in LSU terminology) in pixels with 100% abundance of a specific cover type (and hence 0% of the other types). LSU assumes that the reflectance in a mixed image pixel is the linear combination of these endmember spectra.

Based on these considerations, we divided our algorithm in 4 main parts: 1) image selection, 2) preliminary estimation of water, vegetation and sand pixels, 3) extraction of endmember spectra and estimation of fraction abundance maps using LSU, and 4) aggregation of the abundance maps into blowout surface area (in m^2). We now successively describe the four parts in Section 3.2–3.5, with reference to the algorithm flowchart in Fig. 4 and the graphical representation for an example image of Zuid-Kennemerland in Fig. 5. In Section 3.6 we examine the accuracy of the final result of the algorithm (blowout surface area) using multiple high-resolution orthomosaics collected with an Unoccupied Aerial Vehicle (UAV) at Zuid-Kennemerland (Ruessink et al., 2018).

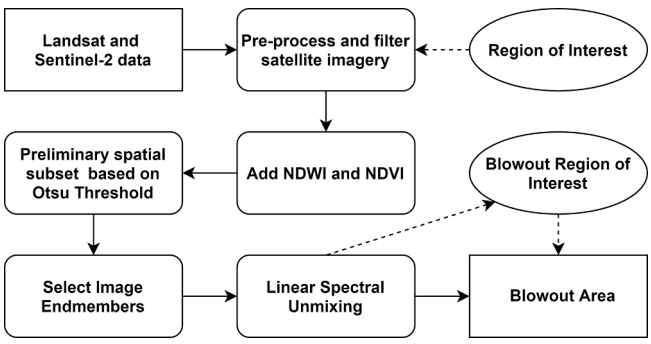

Fig. 4. Flow diagram of the algorithm developed in GEE to quantify the temporal evolution of blowout surface area from medium-resolution Landsat and Sentinel-2 images. All abbreviations are explained in the text.

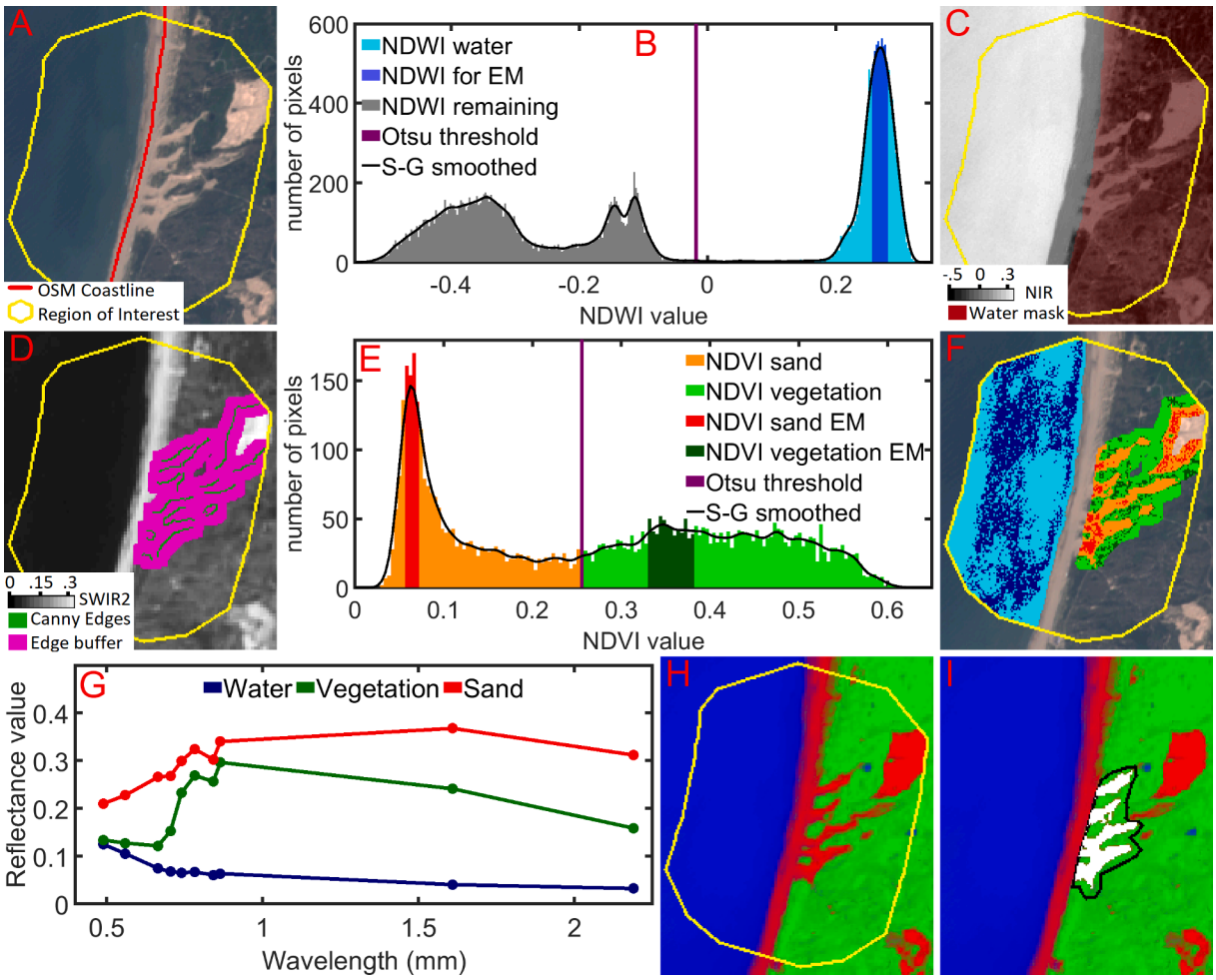

Fig. 5. Example of the adopted GEE workflow based on the Zuid-Kennemerland image shown in the upper left panel A). B) shows its NDWI histogram with the Otsu threshold value, resulting in the land–water image in C). Based on Canny edge detection and a buffer morphological a subset of sand-vegetation pixels (purple in D) is found, from which an NDVI histogram is computed (E). Image endmembers (abbreviated as EM in the legend of panels B and E) are taken around the water (NDWI; dark blue in B), sand (NDVI; red in E) and vegetation (NDVI; dark green in E) peaks. Their locations are shown in F). All blue, orange-red and green colors in F) correspond to those in B) and E). G) shows the estimated endmember reflectance spectra for the three cover features. H) illustrates the results of linear spectral unmixing, with bright blue, red and green being 100% water, sand and vegetation, respectively. I) shows the identified blowout (white pixels; more than 50% sand abundance) inside the blowout region of interest (black line). All abbreviations are explained in the text.

3.2. *Image selection*

For each site a region of interest (ROI) was defined (Figs. 2 and 5A) by applying a buffer around the Openstreetmap coastline (OSM, the Mean High Water Spring line) such that an even proportion of land and water pixels is present in the ROI and the land part contains the entire blowout system. Images that did not cover the entire ROI or had a cloud cover deducted from the metadata exceeding 90% were excluded. Next, images in which the ROI was not contaminated by clouds or cloud shadows were selected. For this, a pixel-based technique was designed based on the idea that the reflectance of the earth's surface fluctuates naturally within a certain range and that reflectance values of clouds and shadows are above and below this range, respectively. The natural reflectance value from the earth's surface was obtained by computing pixel-wise percentile values for the visible (blue, green and red), near-infrared NIR and short-wave infrared (swir1 and swir2) bands using standard percentile reducer functionality available in GEE. This was done for collections of grouped images based on the spectral similarity of the sensor system: 1) Landsat-4, -5 and -7 (Teillet et al., 2001), 2) Landsat-8 and 3) Sentinel-2. The threshold percentiles were subsequently chosen visually such that they are the lowest and highest percentile before cloud shadows and clouds became apparent, respectively. Images were retained in the workflow when the reflectance was within the accepted range of natural reflectance values for each band and all ROI pixels.

The Scan-Line-Corrector (SLC) of the Landsat-7 ETM + sensor failed on 31 May 2003, resulting in missing stripes of pixels. The Landsat-7 collection was the only imagery between the decommission of Landsat-5 and the launch of Landsat-8 satellites and was thus considered an essential part of the data set. Therefore, following Yin et al. (2017), the missing pixel stripes were filled using images acquired at nearby dates from Landsat-5 or -7 that passed the ROI cloud (shadow) check.

3.3. *Preliminary estimation of water, sand and vegetation pixels*

To facilitate the selection of endmember pixels to be used in LSU, we estimated the potential location of water, sand and vegetation using the spectral indices Normalized Difference Water Index (NDWI) and Normalized Difference Vegetation Index (NDVI) in concert with dynamic Otsu thresholding and Canny edge detection.

Firstly, the areas representing water and land (i.e., sand and vegetation) within each image were discriminated using the NDWI (McFeeters, 2007), given by

$$\mathrm{NDWI} = \frac{\mathrm{green} - \mathrm{NIR}}{\mathrm{green} + \mathrm{NIR}}. \quad (1)$$

The NDWI threshold separating water from land was found dynamically using the Otsu method (Otsu, 1979), an automatic threshold procedure that maximizes inter-class variance in the intensity histogram. All pixels with NDWI values below the threshold were labelled land, while all pixels with an NDWI above the threshold were labelled water (Fig. 5B). Because the ROI at each study site was chosen such that water (sea) was present in near equal proportions to land, the NDWI histogram was typically bimodal, a prerequisite for good performance of the Otsu method. Occasionally, successful water-land segmentation was hindered by relief-based shadows in the blowouts misinterpreted as water and by wave breaking-induced foam misinterpreted as land. Accordingly, the land region was expanded by morphological dilation to re-classify the erroneously detected water as land. Subsequently, the 'land' (foam) objects were shrunk by morphological erosion to re-classify them as water. Morphological dilation and erosion are mathematical operations on binary images (here, water $= 0$; land $= 1$) that grow and shrink the regions with foreground (1, land) pixels, respectively (Gonzalez et al., 2020). The extent of this growing and shrinking is controlled by the size and shape of a structuring element, or kernel. Based on the size and shape of the shadow patches we chose a 30-m wide, square kernel in the dilation step. The kernel during erosion was set to a larger size (60–150 m) to re-classify not only foam but also land pixels on the wet intertidal beach into water (see Fig. 5C). The latter is advantageous for the image endmember selection step described in Section 3.4 because wet-sand pixels have a different spectral signature than dry-sand pixels in the blowouts and thus should not be present in the search for sand endmember pixels.

Secondly, to differentiate between vegetation and sand pixels we applied Otsu thresholding on NDVI values in a buffer around the transition between the sand in the blowouts and the surrounding vegetation (Fig. 5D). We preferred this buffer approach over NDVI thresholding of all land pixels because sand and vegetation pixels are then not necessarily equally abundant and Otsu thresholding may fail. The Canny edge detection method was used to find the transition between sand and vegetation in the blowout systems. We applied it on the Short-Wave-Infrared band (2.1–2.3 μm), which has generally been found to represent the largest spectral difference between vegetation and sand (e.g. Provoost et al., 2005). The Canny detector starts with smoothing the image using a Gaussian filter to suppress noise; here, the standard deviation of the filter was set to 0.5. Edges are then detected by looking for gradients above a threshold value of 0.25. Here, this threshold was empirically set as we wished to focus on the general location of the edge rather than on resolving every small detail. In this study, edges with a minimum length of 10 connected pixels were considered to be true edges (Fig. 5D). If no true edges were detected due to, for example, poor illumination during acquisition, the image was excluded from the workflow. A buffer around the detected edges was then applied to estimate a spatial subset with the land covers of vegetation and sand abundant in even proportions. Sand and vegetation were subsequently separated in the entire land part of the image based on the Otsu threshold using the NDVI, given by

$$\mathrm{NDVI} = \frac{\mathrm{NIR} - \mathrm{red}}{\mathrm{NIR} + \mathrm{red}}, \quad (2)$$

of all pixels in the buffer.

3.4. Image endmember selection and linear spectral unmixing

With the preliminary identification of pixels covered by water, sand and vegetation, we proceeded in finding pure pixels for endmember identification. As in De Vries et al. (2021), we assumed that the most frequent index values of these initial estimates represent the homogeneous land covers of interest. For the water image endmember this is the maximum NDWI value inside the histogram of the separated water pixels (Fig. 5B). For vegetation and sand, the NDVI histogram was split in two using the Otsu threshold. The selection of the maxima may be hindered when image histograms are spiky. Therefore, the histograms were smoothed with a Savitzky–Golay filter prior to the detection of the maxima. The image endmembers were then taken as the subset of pixels with index values around the local maxima of NDWI or NDVI with a buffer of 5% on both sides of the peak (Fig. 5E). The pixels in the subsets were thus assumed to be representative of each of the three land cover types during image acquisition (Fig. 5F). The mean spectral values of these pixels was calculated to characterize the endmember reflectance spectra for each of the three land cover features for each single image (Fig. 5G). We note that by using image-specific spectral signatures, temporal variability in these signatures related to seasonal variations in, for example, plant phenology and sand moisture content, is accounted for. Also, as opposed to time–invariant endmember spectra that have been measured in the field or laboratory, variability in atmospheric conditions between acquisition dates and sensor differences in spectral response are handled.

With the derived image-specific endmember reflectance spectra, the fractional abundance of sand, vegetation and water in each pixel (Fig. 5H) can be estimated with linear spectral unmixing (Keshava and Mustard, 2002)

$$R_i = \sum_{k=1}^{M} f_{ik} S_k + \epsilon_i, i = 1, \cdots, N. \quad (3)$$

Here, R_i is the reflectance spectrum at pixel i, M is the number of endmembers (in this case $M = 3$), f_{ik} is the fractional abundance of endmember k at pixel i, S_k is the reflectance spectrum of endmember k, ϵ_i is an error term, and N is the total number of pixels. Our LSU model was constrained such that each $f_{ik} \geqslant 0$ and that in each pixel the sum of three abundances equals 1.

Relief-based shadows cause substantial non-zero water fractions in the deflation basin and on the lateral walls of the blowouts, in this study especially in winter images of Zuid-Kennemerland and Skodbjerge. As these blowout parts are non-vegetated, we modified the fraction of sand f'_{sand} at these two sites into

$$f'_{\mathrm{sand}} = f_{\mathrm{sand}} + f_{\mathrm{water}}, \quad (4)$$

where f_{sand} and f_{water} are the fractions of sand and water that resulted from Eq. (3), respectively. This shadow correction was not applied at Padre Island, where, firstly, shadows were rarely observed and, secondly, actual water was occasionally present in the blowouts due to a rise in water table by, for example, overwash or high precipitation (Jewell et al., 2017).

3.5. Blowout surface area

To facilitate the quantification of the blowout surface area (in m^2) at the three study sites, we defined a Blowout Region of Interest (BROI) within each ROI. The seaward boundary of the BROI was determined manually by connecting the transition between the beach and the vegetated foredune on either side of the blowout, thereby separating the beach from the blowout entrance. The landward BROI boundary was set such that the blowout evolution in the entire time interval of available imagery was captured, including inland migrating parabolic dunes that evolved from blowout lobes, but excluding areas that were permanently vegetated as well as sand areas not belonging to the blowout-parabolic dune systems (e.g., the non-vegetated dune in the northeast corner of the Zuid-Kennemerland ROI; Fig. 2A). On the scale of the coarsest resolution satellite imagery (30 m), the individual blowouts at Zuid-Kennemerland and Skodbjerge study area could not be determined consecutively through time and therefore, a single BROI (e.g., Fig. 5I for Zuid-Kennemerland) encompassing all blowouts simultaneously was chosen. The patches of sand at Padre Island could be monitored

individually as they had sufficient alongshore spacing; the corresponding BROIs were labeled BROI1 to 6 from south to north. Within each BROI and for every single image, the blowout surface area was computed as the product of the number of pixels with a fractional sand abundance exceeding 50% and the pixel area. For simplicity, the term 'blowout surface area' is also used hereinafter for the surface area of a parabolic dune that evolved from a blowout lobe.

3.6. Validation

We validated the methodology using six high-resolution (1 m) Unoccupied Aerial Vehicle (UAV) orthomosaics collected at Zuid-Kennemerland between April 2014 and March 2017 (Ruessink et al., 2018). As the site was highly dynamic over this time interval, satellite imagery taken within 1 month of the UAV flight date were considered for validation only. Accordingly, 36 satellite images were compared to the six UAV orthomosaics, consisting of 15 Landsat-7, 14 Landsat-8 and 7 Sentinel-2A images. Because the UAV orthomosaics did not contain a NIR band, the red-green–blue-based vegetation index ExGminExR (Meyer and Neto, 2008) was used, in combination with Otsu thresholding, to classify each UAV orthomosoaic into a binary sand-vegetation map. Following Ruessink et al. (2018), we manually reclassified artifacts caused by relief-based shadows in blowouts to sand. The validation was performed on both the fractional sand abundances and the blowout surface area. The UAV-based fractional sand abundance at the resolution of the satellite image was computed as the ratio of the number of UAV-pixels classified as sand to the total number of UAV-pixels inside each satellite pixel. This total number equaled 900 (30×30) for LandSat and 100 (10×10) for Sentinel-2 images. In this way the high-resolution binary sand-vegetation maps were aggregated into fractional sand abundance maps at the scale of the satellite image to compare with the LSU-derived sand abundances. The UAV-based blowout surface area was computed as the product of the UAV-pixels inside the BROI classified as sand times the pixel area (1 m^2).

A confusion matrix was constructed to compare the LSU-derived sand abundances to the those computed from the UAV orthomosaics using 10 0.1-wide bins (i.e., fractional sand abundance of $0-0.1 (= 0-10\%), \cdots, 0.9-1.0 (= 90-100\%)$). We found that 40% of the satellite pixels in the BROI had the same LSU- and UAV-aggregated sand abundance and that the sand fractions in over two-third of the pixels (71%) were within 20% of each other. Only 13% of the satellite pixels were in an LSU-bin that differed by more than 50% of the UAV-bin. Visual inspection (e.g., Fig. 6) showed that most of these misclassifications were located in the vicinity of the edges of the depositional lobes. The satellite-UAV comparison further revealed that the blowout areas estimated from the satellite images were close to those estimated from the UAV orthomosaics (see also Fig. 7 below). In case a UAV orthomosaic did not completely cover the BROI (e.g., Fig. 6B), the blowout area was estimated only for BROI part covered by the UAV orthomosaic. Averaged for all images, the satellite and UAV blowout area differed by less than 2%. In nine satellite images the UAV-based blowout area was overestimated by more than 5%, while for 14 satellite images we found an underestimate of more than 5%. Maximum over- and underestimation were 21% and 16%, respectively. In more detail, the Sentinel-2 images provided area estimates closer to UAV ones (99.8% ± 5.5%; mean ± standard deviation) than the Landsat imagery (98.0% ± 9.4%). On the whole, we can thus state that the developed GEE workflow is sufficiently accurate to reliably examine the temporal evolution of blowout area in vegetated foredunes with medium-resolution satellite imagery.

4. Results

4.1. Zuid-Kennemerland

Fig. 7 and Supplementary Video 1 show the time series of blowout surface area at Zuid-Kennemerland together with a number of selected images to visualize how the blowouts evolved spatially. In the 2012–2013 winter the blowout area showed an abrupt change from near 0 to about 100.000 m^2 due to the artificial excavation of the blowouts through the densely vegetated foredune (Section 2.1). The small sand patches observed prior to excavation were mainly related to the beach extending inland (Fig. 7A). After excavation, the temporal variations in blowout area can be divided in gradual (multi-annual) and seasonal (intra-annual) fluctuations. Between 2013 and 2016 the blowout system grew by ≈ 20.000 m^2 per year to a summer-winter averaged value of about 125.000 m^2 in 2016, after which the gradual growth ceased. As illustrated with Fig. 7B–F, the increase in blowout area during the first years after excavation was primarily due to the development and landward growth of depositional lobes. While the southernmost lobe expanded mostly in southeasterly direction, the lobes adjoining the other four blowouts grew in northeasterly direction.

On the seasonal time scale the blowout area was largest at the end of the winter (March–April) and smallest at the end of the summer (August–September). The typical seasonal difference, based on the 3-month moving average of blowout surface area shown as the gray line in Fig. 7, was about 30.000 to 50.000 m^2, which is 1/5 to 1/3 of the winter blowout area values. Some year-to-year variability is visible for both the summer and winter area values; for example, the 2017 winter blowout area was only 140.000 m^2, about 20.000 m^2 less than in the preceding and following winter (Fig. 7). To illustrate the spatial character of the seasonal differences, two Landsat-8 and two Sentinel-2

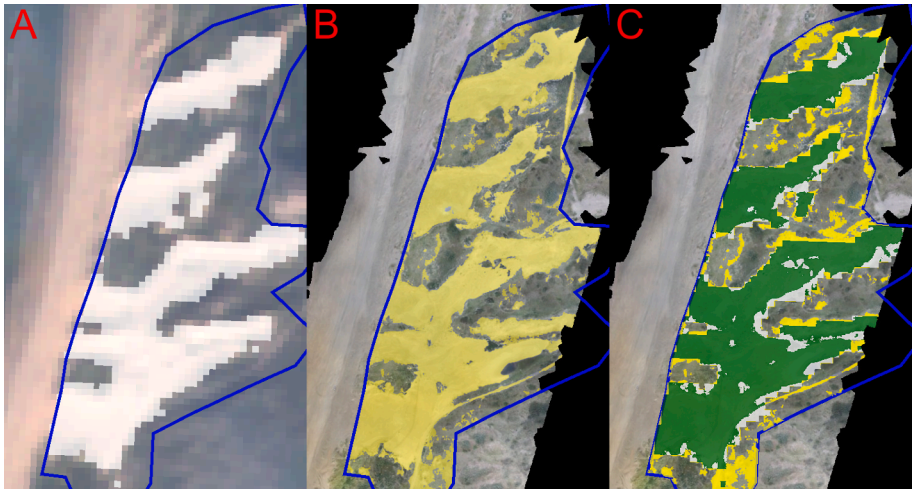

Fig. 6. Example of algorithm validation. (A) Sentinel-2 scene (October 8, 2016) and (B) UAV image (November 3, 2016) with blowout extent in white and yellow, respectively. (C) compares the blowout extents, with green pixels identified identically in the Sentinel-2 and UAV imagery; differently identified pixels have their white (Sentinel-2) and yellow (UAV) color. In (C) the UAV image is given as background. The blue polygon in each panel is the BROI at the Zuid-Kennemerland study site.

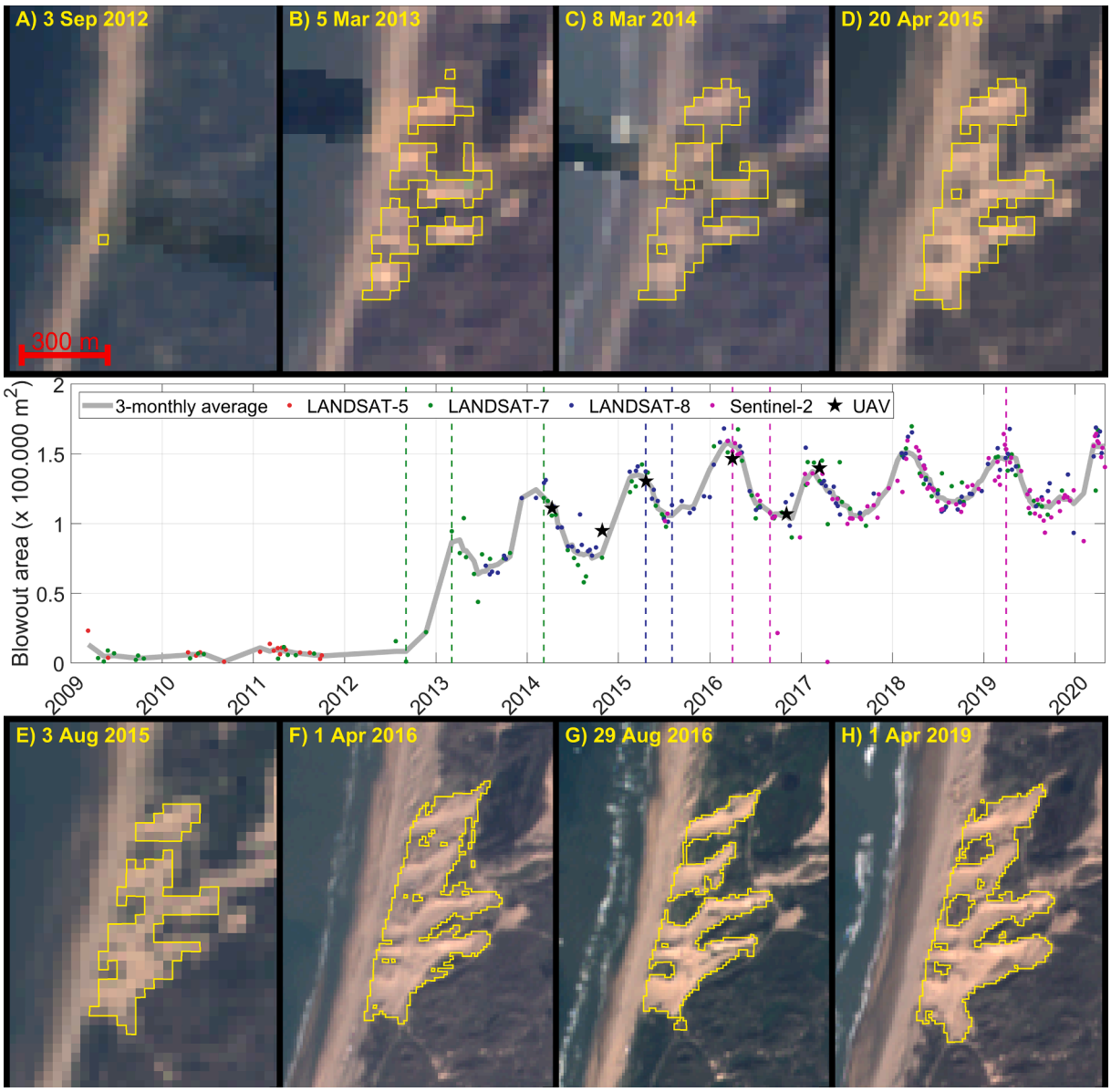

Fig. 7. Blowout surface area over time at Zuid-Kennemerland. The dots are individual estimates of blowout area, the gray line is the 3-month moving average. The tick marks on the *X* axis are, as in all subsequent figures with a time axis, at the start of the year. Panels A) to H) show selected satellite images (A–E are Landsat images; F–H are Sentinel-2 images). The yellow lines in A)–H) are the contours of 50% sand abundance and thus illustrate the perimeter of the blowout system. The acquisition dates of images in panels A) to H) are indicated with vertical dashed lines, color coded as given by the legend for the individual observations. The UAV data collection moments are indicated by the black stars, see Section 3.6. All images are North up.

images are chronologically depicted in Fig. 7D–E and F–G, respectively. As can be seen, the decrease in blowout area between April and August was mainly due to the change from sand to vegetation on the foredune between the blowouts and, to a lesser extent, around the edges of the depositional lobes. The presence of vegetation on the foredune allowed to visually demarcate two northern and the two southern blowouts in the August Landsat images, and of all blowouts in the higher resolution Sentinel-2 image (Fig. 7G). In contrast, none of the blowouts could be distinguished individually in the April images (Fig. 7D and F). Interestingly, towards the end of the study period, the vegetation on the foredune was also visible between the blowouts at the end of winter (Fig. 7H). The resulting local decrease in blowout area was apparently offset by the further landward extension of some of the depositional lobes (for example, compare the lobe southeast of the southernmost blowout in Fig. 7F and H), because, as aforementioned, there was no net gradual change in blowout area in the entire BROI after 2016. Finally, we note that the time series of blowout surface area contains some large outliers, which are seen in Fig. 7 as substantial deviations of individual estimates from the 3-month moving average. We discuss potential causes for these values in Section 5.2.2.

4.2. *Skodbjerge*

As can be seen in Fig. 8 and Supplementary Video 2, the surface area of the blowout system at Skodbjerge also changed gradually and seasonally. The gradual change can be described best using the consecutive summer blowout areas because, as detailed below, the winter values varied greatly from year to year. From 1984 to 2000 the summer blowout area grew from around 40.000 m^2 to 130.000 m^2, equating to an annual growth of about 5.500 m^2. In the subsequent six to seven years the summer blowout area stayed about the same, to then increase to 160.000 m^2 by 2009. From 2009 until 2018 the summer

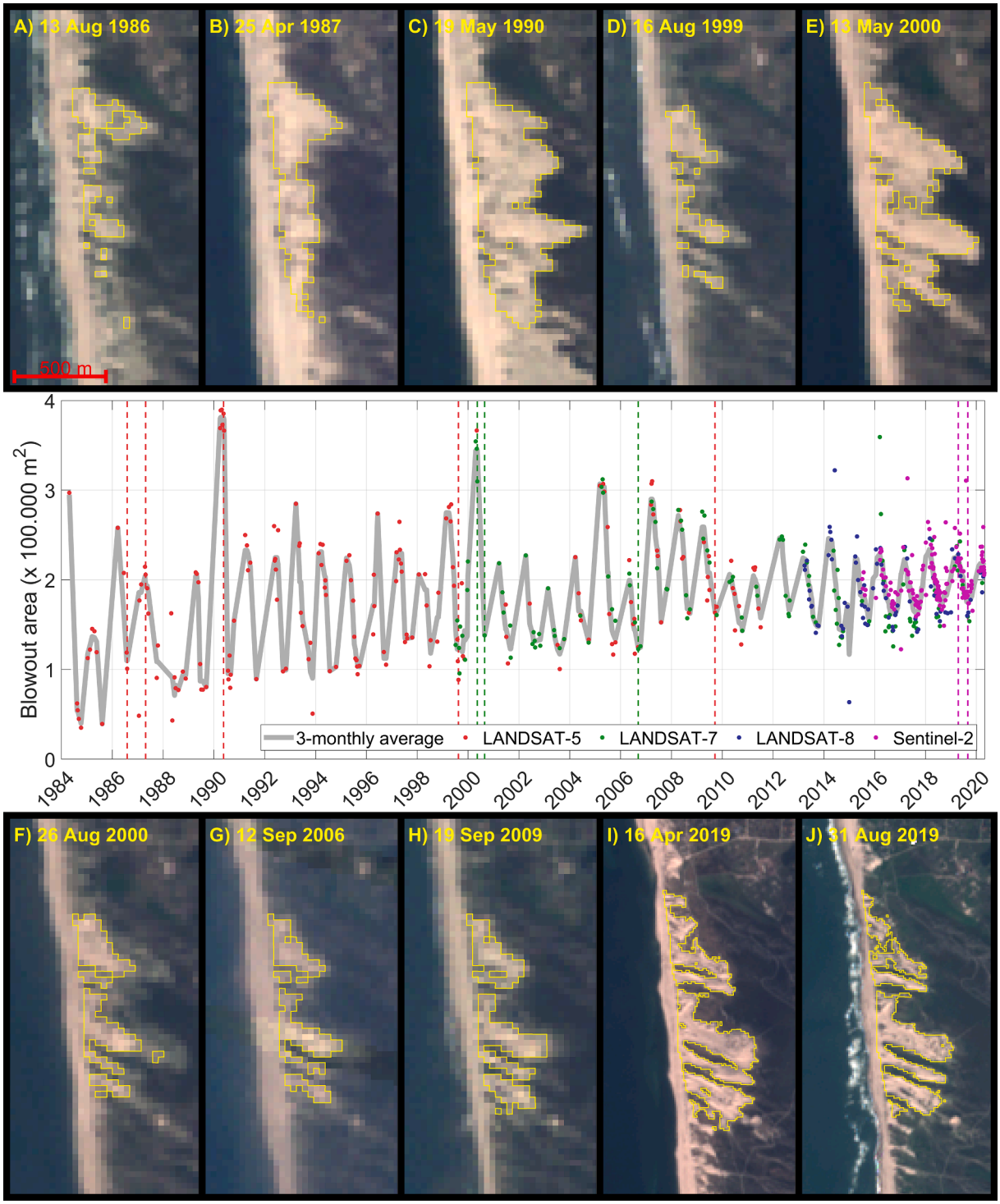

Fig. 8. Blowout surface area versus time at Skodbjerge. The dots are individual estimates, the gray line is the 3-month moving average. Panels A) to J) show selected satellite images (A–H are Sentinel images; I and J are Sentinel-2 images). The yellow lines in A)–J) are the contours of 50% sand abundance. The acquisition dates of images in panels A) to J) are indicated with vertical dashed lines, color coded as given by the legend for the individual observations. All images are North up.

blowout area remained approximately constant again, followed by a minor growth in the final two years (2019–2020). The inter-annual evolution of the blowout systems in these distinct time periods is further illustrated with the satellite images in Fig. 8. In summer 1986 the foredune was locally bare, but it is difficult to indicate if these bare patches can be considered as juvenile blowouts. Between 1987 and 2000 four to five distinctive blowouts developed, with lobes extending to about 300 m inland in east-south-easterly direction (Fig. 8B–F). The widest blowout entrance was found in the north of the study area, a situation that was still present in 2006 (Fig. 8G). In the subsequent years, the lobes of the three southern blowouts grew an additional 100 m landward, while those of the northern blowouts remained relatively stable (Fig. 8H). After 2018 the two southernmost blowouts extended an additional 50 to 100 m inland to reach a cross-shore length of about 450 m (Fig. 8I–J).

During the entire study period the blowout area varied markedly on

the seasonal time scale, especially prior to 2001. In this period, the blowout area was approximately 2–3 times larger in winter compared to the preceding summer with areas ranging from 200.000 to 275.000 m^2. This can be attributed to the alongshore merging and the increasing landward extent of the pixels with less than 50% vegetation cover. This is visible in Fig. 8 by comparing consecutive August with April or May images (Fig. 8A and B). The subsequent increase in vegetation cover toward the summer, as was also observed at Zuid-Kennemerland, was not homogeneously spread within the BROI. Vegetation established especially on the landward extremities of sandy areas and in the entrance of the wide northern blowouts. In the years 1990 and 2000 exceptionally large winter blowout areas were observed, with area estimates going up to 350.000 m^2, almost three times the area of the preceding and consecutive summers. In these winter months, the blowout systems grew to over 500 m inland, with the lobes of the individual blowouts connecting laterally (Fig. 8C and E). As shown for the 2000 case in Fig. 8F, vegetation established at the landward boundary of the lobes and accordingly, the blowout area reduced, although the winter extent of the lobes was visually still detectable. Despite the exceptionally large blowout areas, neither the 1990 nor the 2000 winter resulted in an abrupt change in subsequent seasonal and gradual blowout behaviour. After 2009 the winter blowout area never exceeded 250.000 m^2 again and consequently, the seasonal variations were rather small (on average, about 70.000 m^2) compared to the first 15 years. Vegetation remained visible on the foredune between the three southern blowouts during winters that occurred after 2009 (e.g., Fig. 8I) whereas, as mentioned above, in earlier winters the blowouts were not individually distinguishable.

4.3. Padre Island

The blowouts and parabolic dunes at Padre Island were well separated spatially, which allowed quantifying their individual area evolution over time. As can be seen in Fig. 9 and Supplementary Video 3, the surface area of the six investigated BROIs evolved predominantly in a gradual manner. Seasonal dynamics in surface area was present in most

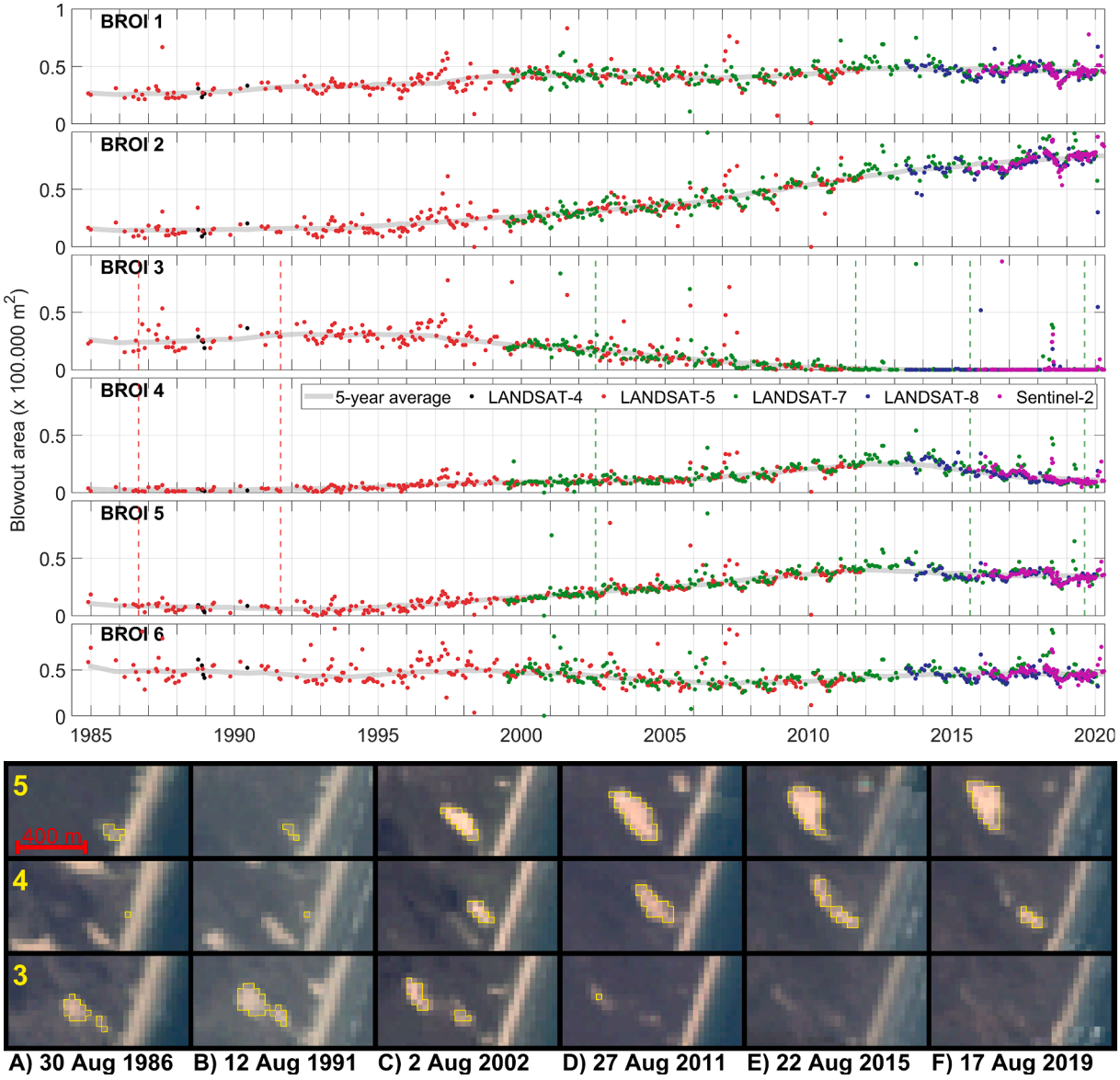

Fig. 9. Blowout surface area versus time at Padre Island. The dots are individual estimates, the gray lines are 5-yr moving averages. Panels A)–F) show selected Landsat satellite images for (from top to bottom) BROIs #5, 4 and 3, which, as elaborated on in the text, display different multi-annual behaviour. The yellow lines in A)–F) are the contours of 50% sand abundance. The acquisition dates of images are indicated with vertical dashed lines in the panels with the blowout area and are color coded as given by the legend for the individual area observations. All satellite images are North up.

BROIs (most notably #2 and 6) after 2006 but with much lower summer-winter amplitudes than at Zuid-Kennemerland and Skodbjerge. No clear seasonal pattern was found prior to 2006. Interestingly, the six time series showed different gradual behaviour. In BROI3 the patch of sand, one of the largest at the beginning of the study period, grew slightly in area up to 1995, to then decline over a period of 15 years, leading to its complete disappearance by 2011 (Fig. 9). The sand patch in BROI1 had approximately the same area in 1985 as in BROI3 but on the contrary, approximately doubled in area to just over 50.000 m^2 in 2017. More pronounced growth was visible in BROIs #2, 4 and 5, mostly after 1995. The growth in BROI2 persisted until the end of the study period, while from 2014 on the area in BROI5 stabilized and that in BROI4 started to decrease at a similar rate as observed in BROI3. Finally, the patch of sand in BROI6, which had the largest area in 1985, barely changed during the entire 35-year study period.

To examine growth, stabilization and decay stages at Padre Island in more detail, we resorted to the satellite imagery for selected blowouts and parabolic dunes (Fig. 9). The sand patch in BROI5 was relatively small (12,000 m^2), rectangular shaped and connected to the beach at the start of the study period (Fig. 9A). Until 1994 this blowout gradually decreased in area (up to around 5,000 m^2) by vegetation colonization, which also detached the blowout lobe from the beach around 1990 (Fig. 9B). From 1995 to 2013, the lobe enlarged by landward expansion in northwesterly direction (Fig. 9C–D). Its seaward extremity remained at the 1995 location until 2007. Then, the lobe started to move inland, to widen alongshore and to develop trailing ridges, suggesting its evolution into a parabolic dune (Fig. 9D–E). This caused the surface area to grow to its maximum of 50,000 m^2 in the summer of 2013. From this moment on, vegetation started to colonize the dune's northeastern and seaward side (Fig. 9E-F), causing an overall decline in surface area. In BROI4 a blowout appeared clearly for the first time in 1991 (Fig. 9B) and remained open to the beach until around 1998. Because of the northwesterly growth of the lobe's landward extremity, the surface area kept on growing until 2014, first by about 700 m^2/yr to 2007 and then faster (3,100 m^2/year) to a maximum area of 34,000 m^2 in spring 2013 and 2014 (Fig. 9). The surface area then decreased due to the encroachment of vegetation on the lobe's landward side (Fig. 9E–F). This landward part became completely overgrown with vegetation in late 2019, while the seaward part remained present until the end of the study period (Fig. 9E–F). Finally, the patch of sand in BROI3 had already lost the open connection to the beach in 1985 (Fig. 9A) and appeared to consist of two parts. From 1991, the seaward part diminished in area while remaining at its location (Fig. 9B–D). Concurrently, the landward part moved in northwesterly direction (Fig. 9B–C). Eventually, this part also became increasingly covered in vegetation (Fig. 9C–D), resulting in an area loss of 2,900 m^2/year between 1997 and 2010 and culminating in its complete disappearance by 2011. The overarching gradual evolution that arises from these selected examples is that (i) a blowout is initially connected to the beach and grows inland even though at some moment in time vegetation grows back in the blowout entrance, (ii) a parabolic dune can evolve from the blowout lobe, and (iii) vegetation eventually covers the entire sand surface.

5. Discussion

5.1. Blowout evolution

5.1.1. Gradual change

In this paper we have developed and applied an algorithm based on linear spectral unmixing to quantify the temporal evolution of the surface area of trough blowouts and resulting parabolic dunes from publicly available medium-resolution satellite imagery. We observed growth, stabilization and decay phases that are reminiscent of the geomorphological, bio-geomorphological and ecological stages in Schwarz et al. (2019)'s conceptual blowout model (Fig. 1). For instance, blowouts with an open connection to the beach widened and lengthened (e.g., at Zuid-Kennemerland and Skodbjerge), corresponding to the geomorphological stage. The limited landward extension of the northernmost blowout at Skodbjerge after 2000 coincided with vegetation encroachment at its seaward entrance, which was not observed for the more southern blowouts at this location. The limited lobe extension and vegetation encroachment may be interpreted as the transition into the bio-geomorphological stage for this particular blowout. Consistent with McKenna (2007), our Padre Island results demonstrate that a blowout lobe can evolve into a parabolic dune and migrate inland for decades even though the bare-sand connection to the beach is lost entirely. Presumably, being disconnected from the beach leads to a slow shift in dominance from abiotic to biotic processes on the deflation basin and in turn, causes a delayed vegetation response compared to that in the blowout entrance. The patches of sand in BROI3 and 4 at this location are the only ones in our observations that became completely vegetated.

Despite the availability of more than 45 years of satellite imagery, a complete growth-stabilization-decay sequence has thus not been observed at any of the three study sites. Only blowout 4 at Padre Island almost exhibited a complete sequence between 1990 and 2020 and accordingly, we estimate the lifespan of a blowout (i.e. completing the growth to decay sequence) at Padre Island to be at least 30 years. Data from all sites combined suggest general blowout lifespans to be many decades longer. Despite expectations from the Schwarz et al. (2019) model, neither abrupt changes in evolutionary phase (e.g., triggered by extreme weather events) nor pronounced phase reversals (e.g., re-activation of a closing blowout) were observed at any of the study sites. On the whole, the results of the three study sites combined thus suggest blowouts to progress through prolonged successive phases of growth, stabilization and decay without any sudden, complicated phase changes.

Blowouts adjacent to each other do not need to be in the same evolutionary phase. This was seen most clearly for Padre Island, but also the individual blowouts at Zuid-Kennemerland and Skodbjerge behaved somewhat differently. Lengthening of the blowouts at these two sites was observed to be more pronounced for blowouts with a relatively narrow width, possibly pointing to stronger funnelling of the wind over the blowout deflation basin and a larger sand throughput. For example, the rather narrow northernmost blowout at Zuid-Kennemerland expanded more landward than the wider blowouts to the south (Fig. 7) and the three individual southern blowouts at Skodbjerge expanded further landward than the wider blowout to the north (Fig. 8). As mentioned at the beginning of this section, limited landward expansion coincided with vegetation encroachment at the blowout's seaward entrance. To explore whether the associated shift from the geomorphological into the bio-geomorphological stage is related to blowout dimension, the width and length of each blowout at Zuid-Kennemerland and Skodbjerge were estimated from two representative satellite images (Fig. 10). Due to limited data resolution we assumed: (1) the entrance-width of alongshore adjacent blowouts with a shared depositional lobe was the sum of both blowouts (blowout 2 at Zuid-Kennemerland); (2) since the deflation basin and the depositional lobe could not be separated, the complete length of the sandy part of the blowout was assessed. Individual blowouts that were observed to lengthen most over the observed period (Zuid-Kennemerland 1 and 5, Skodbjerge 2 and 4) showed a relatively low ratio ($<\approx 1:3$) in entrance width to full blowout length. In contrast, the blowouts that lengthened least had a width-to-length ratio in excess of 1 : 3. These observations might suggest that a low width-to-length ratio implies blowouts to be in their geomorphological state with pronounced wind acceleration, sand throughput and lobe development. A further increase in width-to-length ratio (relatively wider blowouts) might lead to reduced wind acceleration, resulting in stabilization of the blowout surface area. Thus a width-to-length ratio of around 1:3 might mark the transition from blowout growth in the geomorphological phase to stabilization in the bio-geomorphological phase. It is likely that the causes for the transition are more complicated than suggested from the present simple

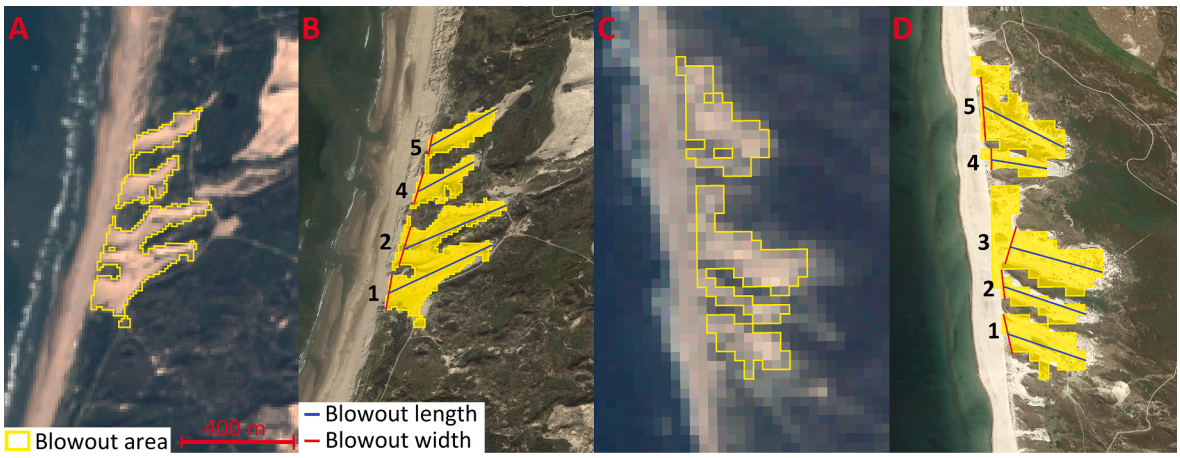

Fig. 10. Example imagery of (A) Sentinel-2A at Zuid-Kennemerland on 29 August 2016 and (C) Landsat-5 at Skodbjerge on 9 September 2008 with (B and D) the width and length of individual blowouts, overlain on a high-resolution Google Earth image of 2021. The width to length ratios are 0.30, 0.37, 0.48 and 0.27 for blowouts 1 to 5 at Zuid-Kennemerland and 0.44, 0.21, 0.41, 0.33 and 0.68 for blowouts 1 to 5 at Skodbjerge. Note that blowout 2 at Zuid-Kennemerland comprises two deflation basins that share the same depositional lobe. All images are North up.

morphometric analysis. The degree of wind acceleration and the resulting blowout evolution may also depend on other aspects of blowout morphology, such as the depth of the deflation basin, the blowout planview (e.g., rectangular or trapezoidal) and blowout axial profile (e.g., concave, linear or convex) (Pye and Blott, 2016; Smyth et al., 2020). Furthermore, Nguyen et al. (2022) proposed that long-term blowout evolution is additionally governed by the orientation of the blowout relative to the dominant wind direction.

5.1.2. Seasonal change

At all three study sites seasonal variations in blowout areas were superimposed to multi-annual trends, with larger blowout areas in winter than in summer. Our results indicate that the magnitude of seasonal variations depends on the latitude of the study area, as they were by far the largest at Skodbjerge (Fig. 8) and virtually absent at Padre Island (Fig. 9). There may be multiple reasons for the observed pronounced summer-winter difference at Skodbjerge and Zuid-Kennemerland. Firstly, it may be induced by seasonal changes in plant development. The growth of European marram grass (*Ammophila arenaria*), one of the dominant plant species at both sites, varies seasonally. Its increased density in summer may explain the change from sand to vegetation on the foredune between the blowouts. During several field visits to the Zuid-Kennemerland blowouts we observed how some groups of buckthorn (*Hippophae rhamnoides*) shrubs were partially buried by landward growing depositional lobes. When these deciduous plants shed their leaves in early winter, the edges of the lobes will be classified as sand. The regrowth of leaves in spring will reverse the classification of the pixels to vegetation, leading to seasonality in blowout surface area. Secondly, in analogy with observations of seasonal sand transport through a trough blowout at Pinery Provincial Park, Canada by Byrne (1997), we may expect the growth of depositional lobes to be most pronounced in winter given the seasonality in the wind climate at both sites (Section 2). What is more, the observed interannual variability in winter blowout area at Zuid-Kennemerland appears to be correlated to interannual variability in wind speed. The about 20.000 m^2 lower winter area in early 2017 (Fig. 7) was observed after a substantially less windy winter. During the preceding and subsequent winters, daily averaged wind speeds at the near-by meteorological station of IJmuiden (see Fig. 3) peaked between 15 and 20 m/s and the 2-month average wind speed values were near 10 m/s. In contrast, in the 2016/2017 winter daily average values were all well below 15 m/s and the 2-month average values were around 6 to 7 m/s. To conclude, our data suggest that seasonal patterns in vegetation biomass (high in summer, low in winter) and in sand transport (high in winter, low in summer) exert an important control on the development of blowout surface areas.

5.1.3. Episodic change

At Skodbjerge, seasonal change in blowout area was superimposed by episodic increases in winter of more than 100.000 m^2 (in 1990, 2000 and 2005). The exceptionally large winter blowout areas are all associated with extreme storms, high surge levels and substantial foredune erosion (Earnshaw and Madsen, 2014). In early 1990 the Danish coast was hit by two storms in close succession (26 January and 27 February), both with a return period near 55 years, while the storm in 2005 had an return period of about 90 years (Earnshaw and Madsen, 2014). Substantial erosion at the blowout mouth, potentially including the removal of incipient dunes, provides a highly efficient pathway for inland sand transport during these severe wind conditions. Storm surges and dune erosion may thus invoke episodic blowout expansion. However, none of the expansions at Skodbjerge caused a persistent change in the long-term evolutionary trend of the blowout system. Interestingly, we did not observe one or more episodic areal increases at Padre Island, even though Jewell et al. (2015) described how specific blowouts at Padre Island were re-activated by storms. Moreover, the impact of Hurricane Bret, which made landfall on Padre Island in August 1999 as a category 3 hurricane, is not noticeable in the time series of blowout area shown in Fig. 9. We thus suggest that the timing of the storm/hurricane season relative to the vegetation season potentially invokes an important control on episodic blowout evolution, with limited impact when a storm coincides with the growth season (as at Padre Island, but not at Skodbjerge).

5.2. Methodological issues

5.2.1. Image endmembers and spectral unmixing

Based on index histograms from potential vegetation, sand and water pixels in individual images we obtained the spectral signatures of endmember pixels for use in the LSU model. The close correspondence between satellite-derived blowout areas and those computed from high-resolution UAV orthomosaics without unmixing provides confidence in our approach. In this subsection we explore the performance of endmember pixel identification and of the LSU model further by examining the location of the selected endmember pixels and the spatial structure of the LSU error term in Eq. (3).

Although pixels used for endmember identification were independently extracted from each image, it may be expected that these pixels were at similar locations over time. As visible in Fig. 11, pixels

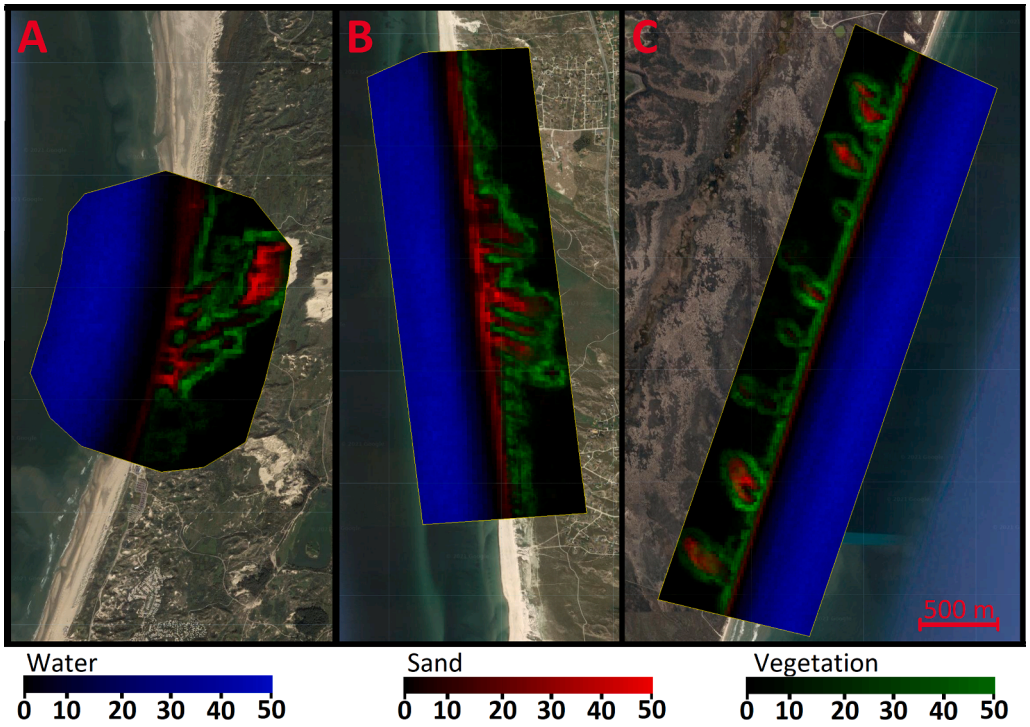

Fig. 11. Location of selected water, sand and vegetation endmember pixels as percentage of the total number of images used at (A) Zuid-Kennemerland, (B) Skodbjerge and (C) Padre Island. Percentages outside the region of interest are 0 by definition, and are therefore not shown. All images are North up.

characterizing the endmember sand were indeed mostly detected within the blowouts or on the upper (dry) beach, while those characterizing vegetation were predominantly detected in the immediate surroundings of the blowouts or on the uninterrupted foredune. The water endmember pixels were distributed more evenly across the sea, with diminishing percentages towards the coastline (Fig. 11). This was expected given the spatially homogeneous spectral character of the water pixels further away from the coastline. Sand pixels at Zuid-Kennemerland were also often extracted from an unvegetated parabolic dune in the northeastern part of the ROI (Fig. 11A). Although this resulted in frequent vegetation endmember identification landward of the blowouts, the inclusion of the unvegetated parabolic dune area was required to ensure a sufficient number of sand endmember pixels in the images collected prior to the excavation of the blowouts in 2013. In summary, Fig. 11 illustrates that the selected endmembers, adapted for inter-scene difference, represented similar parts for either a vegetated, sandy or water surface within the region of interest over time.

The spatial distribution of the root-mean-square (RMS) error in the spectral model fit, a typical measure to illustrate the goodness of the LSU fit (e.g., Painter et al., 1998), was examined for the Zuid-Kennemerland site using satellite imagery collected between 2015 and 2020. Fig. 12 shows the temporal means of the RMS error at each pixel separately for summer (June-August) and winter (November-February). The largest RMS errors were observed (1) on the intertidal beach throughout the year, (2) landward of the BROI during summer and (3) on the south-facing blowout and dune slopes in winter. The high error on the beach

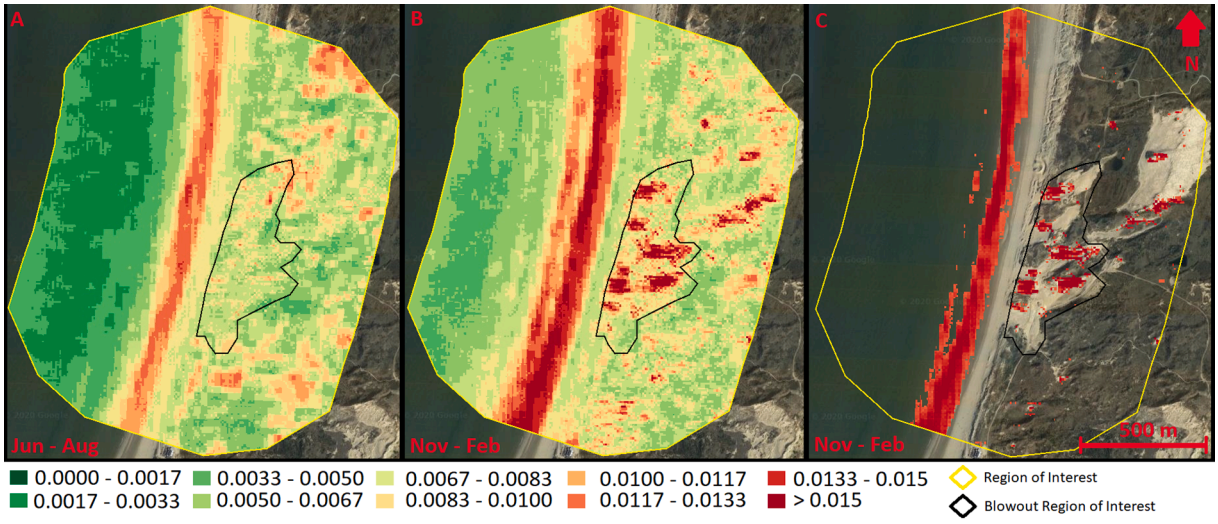

Fig. 12. Temporal mean root-mean-squared error of the mixture model between 2015 and 2020 based on all selected satellite images at Zuid-Kennemerland for (A) summer and (B–C) winter on top of a Google Earth image (2018). (C) shows errors above 0.012 only to better illustrate their location with respect to the blowout relief.

was caused by the presence of white foam resulting from wave breaking. These white-water pixels have different spectral reflectance characteristics than water, sand and vegetation pixels (e.g., Vos et al., 2019) and therefore did not fit well with the endmember spectra. The intertidal area fell well outside the BROI because of the morphological dilation of the water mask (Section 3.3). The higher error in summer was due to vegetation with a different spectral signature ('greener') than near the blowouts. It presumably reflects the common cross-shore zonation in plant species (with different spectral signatures) in coastal dunes (e.g., Maun and Perumal, 1999). Finally, the higher error in winter inside the BROI was due to a combination of the high solar zenith angle in winter and the strong topographic relief of the blowouts. As a consequence, the south-facing slopes were brighter illuminated; the relatively high reflectance values were not contained in the endmember spectra. Still, the sand endmember was the endmember with high reflectance values and thus the south-facing slopes were classified correctly as sand. To summarize, Fig. 12 further illustrates the good performance of our endmember selection approach: resulting RMS errors were highest outside the BROI, while the high RMS errors inside the BROI during winter did not affect the computation of blowout area.

5.2.2. Outliers in blowout surface area

Despite our efforts to remove poor-quality images from the workflow, outliers in blowout surface area at all three study sites remained present (Figs. 7–9). An investigation of the corresponding images shows that degraded image quality due to the presence of cirrus clouds or haze was the main reason for the outliers. The associated reduced spectral difference between sand and vegetation affected endmember selection and resulted in unrealistically small or large blowout area estimates. Misclassifications of the cloud filter also caused several outliers. Blowout area was overestimated from partly cloud-covered images, because clouds have relatively high reflectance values and correspond closely to sand endmember spectra. When cloud shadows covered a relatively large part of the study area, blowout area became unrealistically small as the shadows were included in the water mask. One way to avoid the cloud-induced outliers would have been to include a visual inspection step after the image-selection step; however, this would have gone at the expense of the automated nature of the algorithm and therefore, we did not pursue it. Furthermore, we could have been more strict in selecting the images that we assumed to be cloudfree. This would have removed several outliers, but also some cloudfree images and thus would have reduced the total number of observations. Finally, at Skodbjerge, outliers were additionally due to (i) snow cover eliminating the spectral difference between sand and vegetation, and (ii) extensive shadows due to high solar zenith angle in winter, resulting in shadow pixels being selected as endmembers for sand.

5.2.3. Blowout areal and volumetric change

Our algorithm provides an estimate for blowout surface areas and can inherently not quantify volumetric changes and sand budgets associated with blowout dynamics. Therefore we cannot say how identified episodic, seasonal and gradual changes in blowout area are reflected in temporal volumetric changes at our study sites. Ideally, area fluctuations derived from satellite imagery are complimented with digital models of elevation change computed from repeated topographic surveys with airborne Lidar or UAV photogrammetry. The combined data sets could reveal how areal and volumetric changes relate to each other, and how this relationship changes as the blowout evolves through its bio-geomorphological stages. Moreover, the combined use of areal and volumetric data would be essential elucidating bio-geomorphological thresholds that determine stage transitions (cf. Balke et al., 2014; Eichel et al., 2017). This type of analysis could reveal (i) under which geomorphological activity (sand erosion or deposition) late-successional vegetation-types die off (vegetation to sand transition) or plants can establish on bare sand (sand to vegetation transition); or, (ii) what fractional vegetation cover is needed for plants to start engineering their environment or to stop sand movement altogether. We believe that the quantification of threshold dynamics is a critical step in the further development of bio–geomorphological coastal–landscape models (e.g., Baas and Nield, 2010; Keijsers et al., 2016) for use in scientific and applied projects.

6. Conclusions

The developed automated workflow allows to quantify the temporal evolution of the surface area of foredune trough blowouts and resulting parabolic dunes from medium-resolution multi-spectral satellite imagery available since the mid 1980s. Linear spectral unmixing was applied using endmembers derived from each individual image to extract blowout surface area over time at one man-made blowout system (Zuid-Kennemerland, Netherlands) and two natural systems (Skodbjerge, Denmark; Padre Island, Texas, USA), assigning land pixels with a fractional vegetation cover less than 50% to the blowout. A validation for Zuid-Kennemerland with high-resolution UAV data confirmed the accuracy of our approach. The obtained time series of blowout surface areas show gradual (multi-year), seasonal and episodic (disturbance-recovery) changes, with the magnitude of the changes depending on site-specific characteristics and the evolutionary phase of the blowouts. Observations from all sites combined suggest that blowouts go through prolonged, successive phases of growth, stabilization and decay, resulting in blowout lifetimes of at least multiple decades. These phases are reminiscent of the geomorphological, bio-geomorphological and ecological stages in blowout evolution proposed in earlier work (Schwarz et al., 2019). Reversals in phase (e.g., activation of a decaying blowout) were not observed. Blowouts with a width-to-length ratio less than approximately 1:3 were shown to expand by landward lobe extension, while blowouts with larger ratios tended to stabilize. Multi-annual decay starts after vegetation colonizes the seaward opening of the blowout, with the possibility of the blowout lobe evolving into a parabolic dune before finally becoming fully vegetated. Seasonal fluctuations in blowout area increase markedly with latitude from being almost absent at Padre Island to dominating the signal at Skodbjerge. The larger blowout area in late winter to early spring presumably reflects seasonal plant development and increased lobe extension because of the more energetic wind conditions in winter. Episodic change was observed at Skodbjerge only, and is associated with substantial foredune erosion because of high storm surges during winter. The episodic increase in blowout area did not induce a persistent change in gradual or seasonal blowout dynamics.

Data availability statement

The developed scripts can be found in the online GEE repository https://code.earthengine.google.com/?accept_repo=users/bgruessink/BlowoutSurfaceArea.

CRediT authorship contribution statement

Niels Kuik: Methodology, Software, Formal analysis, Visualization, Writing - original draft, Writing - review & editing. **Job Vries:** Methodology, Visualization, Supervision, Writing - review & editing. **Christian Schwarz:** Conceptualization, Supervision, Writing - review & editing. **Gerben Ruessink:** Conceptualization, Supervision, Writing - original draft, Writing - review & editing, Project administration, Funding acquisition.

Declaration of Competing Interest

The authors declare that they have no known competing financial interests or personal relationships that could have appeared to influence the work reported in this paper.

Acknowledgements

We thank the two anonymous reviewers and Professor Patrick Hesp for their comments, which helped us to add clarity to the methodology and the results, and to provide context. The work described here was initiated as part of the project *Aeolus meets Poseidon: wind-blown sand transport on wave-dominated beaches* (Grant No. 13709; awarded to GR) of the Vici Talent research programme, which is financed by the Dutch Research Council (NWO). JdV and GR acknowledge additional financial support by the NWO WOTRO Joint Sustainability Development Goal Research Program (Grant No. W07.303.106).

Appendix A. Supplementary data

Supplementary Videos 1–3 display the time series of surface area of the blowouts at Zuid-Kennemerland, Skodbjerge and Padre Island, respectively, together with 1 to 2 satellite images per month. These videos can be found, in the online version, at https://doi.org/10.1016/j.aeolia.2022.100812.

References

Abhar, K.C., Walker, I.J., Hesp, P.A., Gares, P.A., 2015. Spatial-temporal evolution of aeolian blowout dunes at Cape Cod. Geomorphology 236, 148–162.
Anderson, J.L., Walker, I.J., 2006. Airflow and sand transport variations within a backshore-parabolic dune plain complex: NE Graham Island, British Columbia, Canada. Geomorphology 77, 17–34.
Arens, S.M., Mulder, J.P.M., Slings, Q.L., Geelen, L.H.W.T., Damsma, P., 2013. Dynamic dune management, integrating objectives of nature development and coastal safety: examples from the Netherlands. Geomorphology 199, 205–213.
Arens, S.M., De Vries, S., Geelen, L.H.W.T., Ruessink, G., Van der Hagen, H.G.J.M., Groenendijk, D., 2020. Comment on 'Is 're-mobilisation' nature restoration or nature desctruction? A commentary' by I. Delgado-Fernandez, R.G.D. Davidson-Arnott & P. A. Hesp. J. Coast. Conserv. 24, 17. doi:10.1007/s11852-020-00731-1.
Baas, A., Nield, J., 2010. Ecogeomorphic state variables and phase-space construction for quantifying the evolution of vegetated aeolian landscapes. Earth Surf. Proc. Land. 35, 717–731. https://doi.org/10.1002/esp.1990.
Balke, T., Herman, P.M.J., Bouma, T.J., 2014. Critical transitions in disturbance-driven ecosystems: identifying Windows of Opportunity for recovery. J. Ecol. 102, 700–708. https://doi.org/10.1111/1365-2745.12241.
Battiau-Queney, Y., 2014. The dunes of Merlimont (north of France): a natural museum of aeolian landforms, in: Coastal dunes management strategies and practices: perspectives and case studies, pp. 51–65.
Byrne, M.L., 1997. Seasonal sand transport through a trough blowout at Pinery Provincial Park, Ontario. Can. J. Earth Sci. 34, 1460–1466.
Carter, R.W.G., Hesp, P.A., Nordstrom, K.F., 1990. Erosional landforms in coastal dunes. chapter 11. pp. 217–250.
Castelle, B., Bujan, S., Ferreira, S., Dodet, G., 2017. Foredune morphological changes and beach recovery from the extreme 2013/2014 winter at a high-energy sandy coast. Mar. Geol. 385, 41–55.
Castelle, B., Laporte-Fauret, Q., Marieu, V., Michalet, R., Rosebery, D., Bujan, S., Lubac, B., Bernard, J.B., Valance, A., Dupont, P., El Moctar, A.O., Narteau, C., 2019. Nature-based solution along high-energy eroding sandy coasts: preliminary tests on the reinstatement of natural dynamics in reprofiled coastal dunes. Water 11, 1–16. https://doi.org/10.3390/w11122518.
Corenblit, D., Baas, A., Balke, T., Bouma, T., Fromard, F., Garófano-Gómez, V., González, E., Gurnell, A.M., Hortobágyi, B., Julien, F., Kim, D., Lambs, L., Stallins, J. A., Steiger, J., Walcker, R., 2015. Engineer pioneer plants respond to and affect geomorphic constraints similarly along water-terrestrial interfaces world-wide. Glob. Ecol. Biogeogr. 24, 1363–1376. https://doi.org/10.1111/geb.12373.
Davidson-Arnott, R.G.D., 2005. Conceptual model of the effects of sea level rise on sandy coasts. J. Coastal Res. 21, 1166–1172.
Dech, J.P., Maun, M.A., Pazner, M.I., 2005. Blowout dynamics on Lake Huron sand dunes: analysis of digital multispectral data from colour air photos. Catena 60, 165–180.
De Vries, J., Van Maanen, B., Ruessink, G., Verweij, P.A., De Jong, S.M., 2021. Unmixing water and mud: Characterizing diffuse boundaries of subtidal mud banks from individual satellite observations. Int. J. Appl. Earth Obs. Geoinf. 95 https://doi.org/10.1016/j.jag.2020.102252.
De Winter, R.C., Gongriep, F., Ruessink, B.G., 2015. Observations and modeling of alongshore variability in dune erosion at Egmond aan Zee, the Netherlands. Coast. Eng. 99, 167–175.
Earnshaw, M.E., Madsen, H.T., 2014. Dune Erosion and Safety along the Lodbjerg-Nymindegab Coast Denmark. techreport. Kystdirektoratet, Lemvig.
Eichel, J., Draebing, D., Klingbeil, L., Wieland, M., Eling, C., Smidtlein, S., Kuhlmann, H., Dikau, R., 2017. Solifluction meets vegetation: the role of biogeomorphic feedbacks for turf-banked solifluction lobe development. Earth Surf. Proc. Land. 42, 1623–1635. https://doi.org/10.1002/esp.4102.
Ettrich, G., Bunting, P., Jones, G., Hardy, A., 2018. Monitoring the coastal zone using earth observation: application of linear spectral unmixing to coastal dune systems in Wales. Remote Sens. Ecol. Conserv. 4, 303–319. https://doi.org/10.1002/rse2.79.
Gares, P.A., 1992. Topographic changes associated with coastal dune blowouts at Island Beach State Park, New Jersey. Earth Surf. Proc. Land. 17, 589–604.
Gares, P.A., Nordstrom, K.F., 1995. A cyclic model of foredune blowout evolution for a leeward coast: Island Beach, New Jersey. Ann. Assoc. Am. Geogr. 85, 1–20.
Gonzalez, R.C., Woods, R.E., Eddins, S.L., 2020. Digital image processing using MATLAB, third ed. Gatesmark Publishing, Knoxville, TN, USA.
Gorelick, N., Hancher, M., Dixon, M., Illyshchenko, S., Thau, D., Moore, R., 2017. Google Earth Engine: planetary-scale geospatial analysis for everyone. Remote Sens. Environ. 202, 18–27.
Hesp, P.A., 1991. Ecological processes and plant adaptations on coastal dunes. J. Arid Environ. 21, 165–191.
Hesp, P.A., 2002. Foredunes and blowouts: Initiation, geomorphology and dynamics. Geomorphology 48, 245–268.
Hesp, P.A., Hyde, R., 1996. Flow dynamics and geomorphology of a trough blowout. Sedimentology 43, 505–525.
Hesp, P.A., Walker, I.J., 2013. Coastal dunes. Academic Press, San Diego, CA. chapter 11. pp. 328–355.
Houser, C., Labude, B., Haider, L., Weymer, B., 2013. Impacts of driving on the beach: Case studies from Assateague Island and Padre Island National Seashores. Ocean Coast. Manag. 71, 33–45. https://doi.org/10.1016/j.ocecoaman.2012.09.012.
Huntington, J.L., Hegewisch, K.C., Daudert, B., Morton, C.G., Abatzoglou, J.T., McEvoy, D.J., Erickson, T., 2017. Climate engine - cloud computing and visualization of climate and remote sensing data for advanced natural resource monitoring and process understanding. Bull. Am. Meteorol. Soc. 2397–2409 https://doi.org/10.1175/BAMS-D-15-00324.1.
Jackson, D.W.T., Costas, S., González-Villanueva, R., Cooper, A., 2019. A global 'greening' of coastal dunes: an integrated consequence of climate change? Global Planet. Change 182, 103026. https://doi.org/10.1016/j.gloplacha.2019.103026.
Jewell, M., Houser, C., Trimble, S., 2015. Initiation and evolution of blowouts within Padre Island National Seashore, Texas. Ocean Coast. Manag. 95, 155–164. https://doi.org/10.1016/j.ocecoaman.2014.04.019.
Jewell, M., Houser, C., Trimble, S., 2017. Phases of blowout initiation and stabilization on Padre Island revealed through ground-penetrating radar and remotely sensed imagery. Phys. Geogr. 38, 556–577. https://doi.org/10.1080/02723646.2017.1338042.
Jungerius, P.D., Van der Meulen, F., 1989. The development of dune blowouts, as measured with erosion pins and sequential air photos. Catena 16, 369–376.
Karlsson, H.V., Larsen, B.G., 2020. Aeolian sediment transport and natural dune development, Skodbjerge, Denmark. Interreg Building-with-Nature North Sea Region, Kystdirektoratet, Lemvig.
Keijsers, J.G.S., de Groot, A.V., Riksen, M.J.P.M., 2016. Modeling the biogeomorphic evolution of coastal dunes in response to climate change. J. Geophys. Res.: Earth Surf. 121, 1161–1181. https://doi.org/10.1002/2015JF003815.
Keshava, N., Mustard, J.F., 2002. Spectral unmixing. IEEE Signal Process. Mag. 19, 44–57.
Kuipers, M., 2014. The daring Dutch: restoring the dynamic dunes. In: Favennac, J., Battiau-Queney, Y. (Eds.), Coastal dunes management strategies and practices: perspectives and case studies, pp. 132–138.
Laporte-Fauret, Q., Castelle, B., Michalet, R., Marieu, V., Bujan, S., Rosebery, D., 2021. Morphological and ecological responses of a managed coastal sand dune to experimental notches. Sci. Total Environ. 782 https://doi.org/10.1016/j.scitotenv.2021.146813.
Luijendijk, A., Hagenaars, G., Ranasinghe, R., Baart, F., Donchyts, G., Aarninkhof, S., 2018. The state of the world's beaches. Sci. Rep. 8, 1–11. https://doi.org/10.1038/s41598-018-24630-6.
Maun, M.A., 1998. Adaptations of plants to burial in coastal sand dunes. Can. J. Bot. 76, 713–738.
Maun, M.A., Perumal, J., 1999. Zonation of vegetation on lacustrine coastal dunes: effects of burial by sand. Ecol. Lett. 2, 14–18.
McFeeters, S.K., 2007. The use of the normalized difference water index (NDWI) in the delineation of open water features. Int. J. Remote Sens. 17, 1425–1432.
McKenna, W., 2007. An evolutionary model of parabolic dune development: blowout to mature parabolic, Padre Island National Seashore, Texas. Master's thesis. Louisiana State University and Agricultural and Mechanical College. URL:https://digitalcommons.lsu.edu/gradschool_theses/4153/.
Meyer, G.E., Neto, J.C., 2008. Verification of color vegetation indices for automated crop imaging applications. Computer and electronics in agriculture 63, 282–293.
Mir-Gual, M., Pons, G.X., Martín-Prieto, J.A., Roig-Munar, F.X., Rodríguez-Perea, A., 2013. Geomorphological and ecological features of blowouts in a western Mediterrean coastal dune complex: a case study of the Es Comú de Muro beach-dune system on the island of Mallorca, Spain. Geo-Mar. Lett. 33, 129–141. https://doi.org/10.1007/s00367-012-0298-7.
Murray, N.J., Phinn, S.R., DeWitt, M., Ferrari, R., Johnston, R., Lyons, M.B., Clinton, N., Thau, D., Fuller, R.A., 2019. The global distribution and trajectory of tidal flats. Nature 565, 222–225. https://doi.org/10.1038/s41586-018-0805-8.
Nguyen, D., Hilton, M., Wakes, S., 2022. Aeolian sand transport thresholds in excavated foredune notches. Earth Surf. Proc. Land. 47, 553–568. https://doi.org/10.1002/esp.5271.
Nordstrom, K.F., Hartman, J.M., Freestone, A.L., Wong, M., Jackson, N.L., 2007. Changes in topography and vegetation near gaps in a protective foredune. Ocean & Coastal Management 50, 945–959.
Otsu, N., 1979. A threshold selection method from gray-level histograms. IEEE Transactions on Systems, Man, and Cybernetics SMC-9, 62–66.

Painter, T.H., Roberts, D.A., Green, R.O., Dozier, J., 1998. The effect of grain size on spectral mixture analysis of snow-covered area from AVIRIS data. Remote Sens. Environ. 65, 320–332.
Pease, P., Gares, P., 2013. The influence of topography and approach angles on local deflections of airflow within a coastal blowout. Earth Surf. Proc. Land. 38, 1160–1169. https://doi.org/10.1002/esp.3407.
Provoost, S., Van Til, M., Deronde, B., Knotters, A., 2005. Remote sensing of coastal vegetation in the Netherlands and Belgium, in: Proceedings 'Dunes and Estuaries 2005' - International Conference on Nature Restoration Practices in European Coastal Habitats, VLIZ Special Publication 19. pp. 139–148.
Pye, K., Blott, S.J., 2016. Dune rejuvenation trials: overview report. Report to Natural Resources Wales. Technical Report KPAL Report 19099. Kenneth Pye Associates Ltd.
Pye, K., Blott, S.J., 2017. Evolution of a sediment-starved, over-stabilized dunefield: Kenfig Burrows, South wales, UK. J. Coast. Conserv. 21, 685–717. https://doi.org/10.1007/s11852-017-0506-8.
Pye, K., Blott, S.J., Forbes, N., Maskell, L.C., 2020. Geomorphological and ecological change in a coastal foreland dune system, Sandscale haws, Cumbria, UK: the management challenges posed by climate change. J. Coast. Conserv. 24, 64. https://doi.org/10.1007/s11852-020-00781-5.
Riksen, M.J.P.M., Goossens, D., Huiskes, H.P.J., Krol, J., Slim, P.A., 2016. Constructing notches in foredunes: effect on sediment dynamics in the dune hinterland. Geomorphology 253, 340–352.
Ritchie, W., 1972. The evolution of coastal sand dunes. Scott. Geogr. Mag. 88, 19–35.
Ruessink, B.G., Arens, S.M., Kuipers, M., Donker, J.J.A., 2018. Coastal dune dynamics in response to excavated foredune notches. Aeolian Res. 31, 3–17.
Schwarz, C., Brinkkemper, J., Ruessink, G., 2019. Feedbacks between biotic and abiotic processes governing the development of foredune blowouts: a review. J. Mar. Sci. Eng. 7, 2. https://doi.org/10.3390/jmse7010002.
Smyth, T.A.G., Jackson, D.W.T., Cooper, J.A.G., 2013. Three dimensional airflow patterns within a coastal trough-bowl blowout during fresh breeze to hurricane force winds. Aeolian Res. 9, 111–123.
Smyth, T.A.G., Delgado-Fernandez, I., Jackson, D.W.T., Yurk, B., Rooney, P., 2020. Greedy parabolics: Wind flow direction within the deflation basin of parabolic dunes is governed by deflation basin width and depth. Prog. Phys. Geogr. 44, 643–660. https://doi.org/10.1177/0309133319899306.
Smyth, T.A.G., Thorpe, E., Rooney, P., 2020. Blowout evolution between 1999 and 2015 in Ainsdale Sand Dunes National Nature Reserve, England. North West Geography 20, 1–13.
Teillet, P.M., Barker, J.L., Markham, B.L., Irish, R.R., Fedosejevs, G., Storey, J.C., 2001. Radiometric cross-calibration of the Landsat-7 ETM and Landsat-5 TM sensors based on tandem data sets. Remote Sens. Environ. 78, 39–54.
Vos, K., Splinter, K.D., Harley, M.D., Simmons, J.A., Turner, I.L., 2019. Coastsat: A Google Earth Engine-enabled Python toolkit to extract shorelines from publicly available satellite imagery. Environ. Modell. Softw. 122, 104528 https://doi.org/10.1016/j.envsoft.2019.104528.
Yan, N., Baas, A.C.W., 2015. Parabolic dunes and their transformations under environmental and climatic changes: Towards a conceptual framework for understanding and prediction. Global Planet. Change 124, 123–148. https://doi.org/10.1016/j.gloplacha.2014.11.010.
Yancho, J.M.M., Jones, T.G., Gandhi, S.R., Ferster, C., Lin, A., Glass, L., 2020. The Google Earth Engine Mangrove Mapping Methodology (GEEMMM). Remote Sens. 12, 3758. https://doi.org/10.3390/rs12223758.
Yin, G., Mariethoz, G., McCabe, M.F., 2017. Gap-filling of Landsat 7 imagery using the direct sampling method. Remote Sens. 9 https://doi.org/10.3390/rs9010012.